

Glutamatergic neurons in the lateral periaqueductal gray mediate wakefulness and REM sleep through different pathways

Yi-Qun Wang

Fudan University

Lei Li

Fudan University

Jian-Bo Jiang

Fudan University <https://orcid.org/0000-0002-0127-7306>

Sebastien Arthaud

UMR 5292 CNRS/U1028 INSERM, Team

Pierre-Hervé Luppi

UMR 5292 CNRS/U1028 INSERM, Center of Research in Neuroscience of Lyon (CRNL), SLEEP Team, Université Claude Bernard Lyon I, Faculté de Médecine RTH Laennec, 7 Rue Guillaume Par

<https://orcid.org/0000-0002-0503-423X>

Zhi-Li Huang (✉ huangzl@fudan.edu.cn)

School of Basic Medical Sciences, State Key Laboratory of Medical Neurobiology and MOE Frontiers Center for Brain Science, Institutes of Brain Science, Fudan University <https://orcid.org/0000-0001-9359-1150>

Article

Keywords: lateral periaqueductal gray, locus coeruleus, rapid eye movement sleep, sublaterodorsal tegmental nucleus, ventral gigantocellular reticular nucleus, wakefulness

Posted Date: June 6th, 2022

DOI: <https://doi.org/10.21203/rs.3.rs-1650527/v1>

License: © ⓘ This work is licensed under a Creative Commons Attribution 4.0 International License.

[Read Full License](#)

1 **Glutamatergic neurons in the lateral periaqueductal gray mediate wakefulness**
2 **and REM sleep through different pathways**

3

4 Yi-Qun Wang¹, Lei Li¹, Jian-Bo Jiang¹, Sébastien Arthaud², Pierre-Hervé Luppi² and
5 Zhi-Li Huang¹

6

7 ¹Department of Pharmacology, School of Basic Medical Sciences; State Key
8 Laboratory of Medical Neurobiology and MOE Frontiers Center for Brain Science, and
9 Institutes of Brain Science, Fudan University, Shanghai 200032, China. ²SLEEP Team,
10 CNRS UMR 5292, INSERM U1028, Faculté de Médecine RTH Laennec, Centre de
11 Recherche en Neurosciences de Lyon (CRNL), Université Claude Bernard Lyon 1,
12 Lyon 69008, France.

13 These authors contributed equally: Yi-Qun Wang, Lei Li.

14 Correspondence and requests for materials should be addressed to Y.-Q.W. (email:
15 yiqunwang@fudan.edu.cn), P.-H.L. (email: luppi@sommeil.univ-lyon1.fr) or Z.-L.H.
16 (email: huangzl@fudan.edu.cn)

17 **Abstract**

18 The lateral periaqueductal gray (LPAG) is essential for coordinating active and passive
19 defensive behaviors which rely on heightened arousal, but its impact on sleep–wake
20 regulation remains unknown. Here, by using targeted recombination in active
21 populations transgenic mouse tool along with neuroanatomical approaches, we first
22 show that two different populations of glutamatergic neurons are activated during
23 wakefulness and rapid eye movement (REM) sleep in the LPAG. Fiber photometry
24 showed that most LPAG vesicular glutamate transporter 2 (Vglut2) neurons are
25 preferentially active during wakefulness. Chemogenetic and optogenetic activation of
26 LPAG^{Vglut2} neurons strongly enhanced arousal associated with immobility. The
27 wakefulness- and immobility-promoting effects of LPAG^{Vglut2} neurons are mediated by
28 their projections to the locus coeruleus and ventral gigantocellular reticular nucleus, as
29 supported by optogenetic manipulations. In contrast, chemogenetic inhibition of
30 LPAG^{Vglut2} neurons reduced REM sleep and increased non-REM sleep. Most LPAG
31 neurons activated during REM sleep hypersomnia and showed descending projections
32 to the sublateralodorsal tegmental nucleus. These findings revealed that two different
33 LPAG^{Vglut2} populations of neurons and circuits induce wakefulness associated with
34 immobility and REM sleep.

35 **Keywords:** lateral periaqueductal gray; locus coeruleus; rapid eye movement sleep;
36 sublateralodorsal tegmental nucleus; ventral gigantocellular reticular nucleus;
37 wakefulness

38 **Introduction**

39 When confronted with dangerous situations, animals, including humans, use several
40 active and passive coping strategies that rely on defensive behaviors^{1, 2}. Active
41 defensive responses, such as fight-or-flight reactions, rely on heightened arousal and
42 skeletal muscle activation, which allows the animal to remain alert. In addition, passive
43 defensive responses, including quiescence and freezing, also depend on wakefulness³.
44 Arousal is the first, necessary step in the activation of the defense cascade in both
45 animals and humans⁴. Recent studies showed that the lateral periaqueductal gray
46 (LPAG) is the midbrain structure essential for coordinating the active and passive
47 defensive reactions to threatening stimuli^{5, 6, 7}. However, whether and how the LPAG
48 participates in sleep–wake regulation remains unclear.

49 Previous clinical and animal studies showed that LPAG has multiple functions,
50 including defensive behaviors, pain and analgesia, cardiovascular control, breathing,
51 maternal behaviors, and reward^{8, 9, 10, 11, 12, 13}. The LPAG ensures survival by generating
52 an appropriate response to threats and mediates the fundamental, rigid motor modes of
53 flight or fight, e.g., attack, running, treading, and/or burying¹⁴. Activation of the efferent
54 projections from the lateral parabrachial nucleus to the LPAG drives the escape
55 behaviors¹⁵. Moreover, the auditory cortex controls noise-evoked escape through a
56 direct excitatory projection to LPAG glutamatergic neurons¹⁶. A preferential projection
57 from the vesicular glutamate transporter 2 (Vglut2) neurons of the ventromedial
58 hypothalamus to the LPAG^{Vglut2} neurons is selectively used during the attack, and it
59 exhibits short-latency and time-locked spikes associated with jaw muscle activity

60 during biting⁸. Vesicular gamma-aminobutyric acid (GABA) transporter neurons in the
61 LPAG are required to detect, chase and attack the prey, while LPAG^{Vglut2} neurons are
62 selectively used for the attack in the mouse hunting behavior¹⁴. These studies suggest
63 that LPAG may have a key role in the defensive system, which relies on heightened
64 arousal. Furthermore, at the neuroanatomical level, the LPAG has functional
65 connections with the central amygdala, hypothalamus, medial prefrontal cortex, lower
66 brainstem, and spinal cord, which are crucial to the sleep–wake cycle^{8, 15, 17}. A
67 substantial number of c-Fos positive neurons were observed in the LPAG after REM
68 sleep deprivation and hypersomnia. In contrast to neurons localized in the ventrolateral
69 periaqueductal gray (VLPAG), which are mainly GABAergic, the LPAG neurons do
70 not express glutamate decarboxylase and are therefore not GABAergic¹⁸. Therefore, we
71 hypothesized that the glutamatergic neurons in the LPAG might play an important role
72 in sleep–wake regulation.

73 In the present study, by using targeted recombination in active populations (TRAP)
74 transgenic mouse tool and c-Fos immunostaining with in situ hybridization techniques,
75 we observed that two different populations of glutamatergic neurons in the LPAG are
76 active during wakefulness and REM sleep. Then, fiber photometry was used to
77 determine the LPAG glutamatergic neurons activity across the spontaneous sleep–wake
78 cycle. *In vivo* and *in vitro* optogenetic and chemogenetic approaches, along with
79 polysomnographic recordings, were used to assess the role of LPAG glutamatergic
80 neurons in wakefulness and rapid eye movement (REM) sleep. Patch-clamp recordings
81 combined with optogenetics were used to investigate the functional connections

82 between LPAG glutamatergic neurons and neurons in the locus coeruleus (LC), ventral
83 gigantocellular reticular nucleus (GiV), and sublateralodorsal tegmental nucleus (SLD).
84 Our results revealed that LPAG glutamatergic neurons differential projections are
85 essential for wakefulness associated with immobility and REM sleep.

86 **Results**

87 **The glutamatergic neurons in the LPAG are activated during wakefulness and**

88 **REM sleep hypersomnia.** TRAP2 transgenic mice were used to identify the LPAG

89 neurons that are activated during wakefulness and REM sleep. After 4-

90 hydroxytamoxifen (4-OHT) injection (Supplementary Fig. 1a), tdtomato labeling (so-

91 called TRAPing) was induced in activated neurons during wakefulness or REM sleep.

92 Neurons activated during wakefulness or REM sleep immediately before perfusion

93 expressed c-Fos. Under three conditions (wake-wake, wake-REM sleep rebound

94 [RSR], and RSR-RSR [Supplementary Fig. 1b]), we investigated the distribution of

95 tdtomato⁺ and c-Fos⁺ neurons in the LPAG (Supplementary Fig. 1c, d). The average

96 numbers of tdtomato⁺ and c-Fos⁺ neurons in the LPAG of wake-wake mice were $45 \pm$

97 4 and 62 ± 8 , respectively (Supplementary Fig. 1e), whereas the average number of

98 double-labeled (tdtomato⁺ and c-Fos⁺) cells was 16 ± 1 . This accounts for

99 approximately 34.7% of the tdtomato⁺ neurons and 25.3% of the c-Fos⁺ neurons

100 (Supplementary Fig. 1e). In the wake-RSR mice, the numbers of tdtomato⁺ cells and

101 c-Fos⁺ cells in the LPAG were 46 ± 2 and 40 ± 1 , respectively (Supplementary Fig. 1e);

102 in this group, the number of double-labeled (tdtomato⁺ and c-Fos⁺) neurons was 8 ± 1 ,

103 which accounted for 21.21% of the tdtomato⁺ cells and 18.22% of the c-Fos⁺ cells

104 (Supplementary Fig. 1e). In the PSR-PSR animals, an average of 47 ± 5 tdtomato⁺ and

105 48 ± 3 c-Fos⁺ cells were observed in the LPAG. The number of double-labeled neurons

106 was 9 ± 1 , which accounted for 21.21% of the mCherry⁺ cells and 18.22% of the c-

107 Fos⁺ neurons (Supplementary Fig. 1e). These findings suggest that the neurons

108 activated during wakefulness and REM sleep belong to two different populations,
109 excepting 20% of the neurons which are activated during both states.

110 Then, to determine the distribution and number of LPAG glutamatergic neurons
111 activated during REM sleep deprivation and rebound periods, we quantified the number
112 of neurons that were immunopositive for c-Fos and Vglut2 in all PAG subdivisions in
113 control (RSC), REM sleep-deprived (RSD), and RSR rats (Fig. 1a). The LPAG
114 contained a higher number of c-Fos-Vglut2 double-labeled neurons in RSD and RSR
115 animals compared to RSC ones (Fig. 1b–g). The numbers of c-Fos cells were
116 significantly larger in the LPAG of RSD (65.50 ± 9.10) ($t = 7.762$) and RSR ($61.25 \pm$
117 10.09) ($t = 8.114$) animals than in RSC animals (Fig. 1g). The double-labeled neurons
118 in RSD and RSR rats constituted 49.35% and 47.83%, respectively, of the c-Fos+
119 neurons detected in the LPAG (Fig. 1g). These results indicate that half of the neurons
120 localized in the LPAG that are activated during RSD and RSR are glutamatergic.
121 Previous studies showed that RSD animals spent significantly less time in REM sleep
122 and more time in wakefulness than the RSR and RSC animals¹⁹; therefore, our results
123 combined with those obtained in the TRAP mice indicate that two different populations
124 of glutamatergic neurons in the LPAG are activated during wakefulness and REM sleep.

125

126 **Population activity of LPAG^{Vglut2} neurons is enhanced during wakefulness.** To
127 study the real-time physiological activities of LPAG glutamatergic neurons during
128 spontaneous sleep–wake cycles, we recorded the LPAG^{Vglut2} neuron calcium activity
129 using fiber photometry in mice. Cre-dependent adeno-associated virus (AAV)

130 expressing the fluorescent calcium indicator GCaMP6f (AAV-Ef1 α -DIO-GCaMP6f)
131 was unilaterally injected into the LPAG of Vglut2-Cre mice, and an optical fiber was
132 implanted into the LPAG (Fig. 2a). GCaMP6f signals and electroencephalography
133 (EEG)/electromyography (EMG) were simultaneously recorded in freely moving mice
134 within their home cages. We found that most GCaMP6f-expressing cells were located
135 in the LPAG (Fig. 2b). Changes in the activity of the LPAG^{Vglut2} neurons were
136 significantly and consistently increased during wakefulness compared to REM sleep (P
137 < 0.0001) and non-REM (NREM) sleep ($P < 0.0001$) (Fig. 2c, d). LPAG^{Vglut2} neurons
138 exhibited significantly lower GCaMP6f activity during NREM sleep, while they
139 displayed medium activity during REM sleep and higher activity during wakefulness
140 (Fig. 2c, d). Notably, LPAG^{Vglut2} neurons showed significantly increased activity
141 immediately before NREM-to-wake, NREM-to-REM, and REM-to-wake transitions;
142 in addition, these neurons had slightly reduced activities before the wake-to-NREM
143 transition (Fig. 2e). These results revealed that the majority of LPAG^{Vglut2} neurons are
144 specifically activated during wakefulness, less active during REM sleep and inactive
145 during NREM sleep.

146

147 **Chemogenetic activation of LPAG^{Vglut2} neurons promotes wakefulness and**
148 **immobility.** We tested the effect of chemogenetic activation of LPAG^{Vglut2} neurons by
149 injecting AAV-hSyn-DIO-hM3Dq-mCherry bilaterally in the LPAG of Vglut2-Cre
150 mice (Fig. 3a, b). *In vitro* electrophysiological experiments showed that current
151 injection in a non-spontaneous-firing hM3Dq-positive Vglut2 neuron induced

152 membrane depolarization (Fig. 3c). Using whole-cell current-clamp recording, we
153 found that CNO administration induced the depolarization of LPAG^{Vglut2} neurons and
154 generated action potentials (Fig. 3d). Application of CNO to the LPAG^{Vglut2} neurons
155 significantly increased the firing frequency and membrane potential (Fig. 3e, f).
156 Furthermore, strong c-Fos expression was found in hM3Dq-expressing (mCherry+)
157 neurons after *in vivo* injection of CNO, showing strong activation of the LPAG^{Vglut2}
158 neurons (Fig. 3g–j).

159 The EEG/EMG recordings showed that CNO injection increased wakefulness and
160 decreased NREM and REM sleep compared to vehicle group administration (Fig. 3k,
161 l). Importantly, chemogenetic activation of LPAG^{Vglut2} neurons strongly enhanced
162 wakefulness and concomitantly reduced both NREM and REM sleep for 7 h after CNO
163 (1 mg/kg) injection at 09:00 in the morning, compared to the vehicle control (Fig. 3m).
164 The duration of wakefulness during 09:00–16:00 increased by 195.20% ($P < 0.0001$),
165 along with an 87.07% ($P < 0.0001$) decrease in NREM sleep and a 97.11% ($P < 0.0001$)
166 decrease in REM sleep (Fig. 3n). To evaluate the effects of chemogenetic activation on
167 EEG activity, we compared the normalized EEG power spectrum of wakefulness,
168 NREM, and REM sleep (Fig. 3o). Compared to vehicle, CNO administration led to an
169 increase in the EEG activity during wakefulness in the frequency range of 7–11 Hz,
170 corresponding to the theta wave band, and a decrease in the range of 0–2.75 Hz (delta
171 waves) (Fig. 3o). The EEG power spectrum of NREM and REM sleep was compared,
172 but no statistical differences were observed between vehicle and CNO groups (Fig. 3o).
173 These analyses suggest that activation of LPAG^{Vglut2} neurons induced an increase in

174 wakefulness with theta oscillations.

175 To better characterize the sleep–wake behaviors in mice, we measured the EMG
176 amplitude during wakefulness (EMG_{Wake}) and compared it between vehicle and CNO
177 groups. Compared to the vehicle group, mice in the CNO group displayed significantly
178 decreased EMG_{Wake} levels ($P = 0.0432$) (Fig. 3p). The ratio of the EMG amplitude
179 during wakefulness after treatment (EMG_{T-Wake}) and that during normal wakefulness
180 (EMG_{N-Wake}) was significantly lower in the CNO group than vehicle group ($P = 0.0083$)
181 (Fig. 3q). Furthermore, we evaluated the effects of the activation of $LPAG^{Vglut2}$ neurons
182 on behavior through the observation of locomotor activity after administering either the
183 vehicle or CNO. Chemogenetic activation of $LPAG^{Vglut2}$ neurons decreased locomotor
184 activity in the open field experiment ($P = 0.0279$) (Fig. 3r, s), suggesting decreased
185 exploratory behaviors. In particular, activation of the $LPAG^{Vglut2}$ neurons by CNO
186 administration was associated with increased immobility time ($P < 0.0001$) (Fig. 3t).

187 Taken together, the results demonstrate that chemogenetic activation of $LPAG^{Vglut2}$
188 neurons induced wakefulness, decreased exploratory behavior, and increased
189 immobility.

190

191 **Optogenetic activation of $LPAG^{Vglut2}$ neurons promotes wakefulness and**
192 **immobility.** Next, we performed optrode recording to precisely stimulate the
193 $LPAG^{Vglut2}$ neurons and determine whether it could initiate arousal. AAVs expressing
194 channelrhodopsin-2 (AAV-DIO-ChR2-mCherry) were stereotaxically injected into the
195 LPAG (Fig. 4a–c). Subsequently, whole-cell patch-clamp recordings of the $LPAG^{Vglut2}$

196 neurons were performed during optogenetic activation. Brief blue light pulses (5 ms)
197 induced single action potentials in Vglut2 neurons, which expressed ChR2 (Fig. 4d).
198 Light pulses were able to evoke action potentials with high-frequency fidelity between
199 1 and 100 Hz (Fig. 4e, f). After the beginning of steady NREM sleep, we performed
200 optical blue light stimulation (473 nm, 5 ms, 30 Hz). Compared to yellow light (589
201 nm), acute blue light stimulation of the LPAG^{Vglut2} neurons induced instant transitions
202 from NREM sleep to wakefulness (Fig. 4g, j). The probability of transition between
203 each pair of sleep–wake stages indicated that optical blue light activation enhanced the
204 probability of inducing wakefulness, along with a simultaneous decrease in the
205 probability to enter NREM or REM sleep (Fig. 4h–l). Short latencies were also
206 observed for sleep-to-wake transitions during blue light pulses at frequencies ranging
207 from 20 to 50 Hz (Fig. 4m). Acute blue light stimulation of the LPAG^{Vglut2} neurons
208 during wakefulness induced a decrease in the EEG activity in the frequency range of
209 0.75–4.25 Hz and 5–7.5 Hz, and an increase in the frequency range of 8–13.75 Hz (i.e.,
210 theta waves) (Fig. 4n). The EMG_{Wake} was determined before and after blue light
211 stimulation. Blue light photostimulation significantly decreased the EMG_{Wake} level (P
212 = 0.0257) (Fig. 4o). The ratio of the EMG_{T-Wake} during wakefulness after treatment with
213 photostimulation and the EMG_{N-Wake} that during the normal wakefulness stage was
214 significantly lower in the blue light group than in unstimulated normal counterparts (P
215 = 0.0164) (Fig. 4p). Importantly, photostimulation of LPAG^{Vglut2} neurons also promoted
216 immobility ($P = 0.0018$) (Fig. 4q). Sustained activation of LPAG^{Vglut2} neurons via long-
217 term optogenetic stimulation (5-ms pulses at 30 Hz, with 40-s on/20-s off for 60 cycles)

218 for 1 h consistently maintained wakefulness and reduced NREM and REM sleep, in
219 LPAG^{Vglut2}-ChR2 mice compared to the baseline control group (Fig. 4r–t). In addition,
220 the amount of wakefulness was increased by 1.50-fold ($P = 0.0099$), with a 69.81% (P
221 = 0.0196) decrease in NREM sleep and a 100.00% ($P = 0.0078$) decrease in REM sleep
222 during 1 h (Fig. 4u).

223 These results indicate that the optogenetic stimulation of LPAG^{Vglut2} neurons is
224 sufficient for initiating and maintaining wakefulness characterized by a decrease in
225 movements and an increased immobility.

226

227 **Anterograde tracing of LPAG^{Vglut2} neurons.** To identify the neuronal pathway
228 underlying the effect of LPAG^{Vglut2} neurons in the sleep–wake cycle, we used a
229 validated conditional anterograde tract (AAV-hSyn-DIO-hrGFP) tracing approach
230 (Supplementary Fig. 2a). The injection site (Supplementary Fig. 2b, c) was validated
231 by the local expression of hrGFP in the LPAG. The projecting axons of LPAG^{Vglut2}
232 neurons were observed in the subparafascicular thalamic nucleus (SPF)
233 (Supplementary Fig. 2d), precommissural nucleus (PrC) (Supplementary Fig. 2e),
234 superior cerebellar peduncle (scp), sublaterodorsal tegmental nucleus (SLD)
235 (Supplementary Fig. 2f), lateral parabrachial nucleus (LPB) (Supplementary Fig. 2g),
236 locus coeruleus (LC) (Supplementary Fig. 2h), and ventral part of gigantocellular
237 reticular nucleus (GiV) (Supplementary Fig. 2i). The LPAG^{Vglut2} neuronal outputs in
238 the brain are summarized in Supplementary Fig. 2j. These findings indicate that
239 LPAG^{Vglut2} neurons project to the LC, SLD, and GiV, which regulate wakefulness and

240 REM sleep.

241

242 **LPAG^{Vglut2} neurons induce wakefulness and immobility through the LC pathway.**

243 To identify the functional role of the projection targets of LPAG^{Vglut2} neurons, we used

244 *in vivo* and *in vitro* optogenetic approaches to precisely activate the LPAG^{Vglut2}-LC

245 pathway. Then, we injected the AAV-DIO-ChR2-mCherry construct into the LPAG with

246 optical fibers targeting the axonal terminals in the LC of Vglut2-Cre mice (Fig. 5a–c).

247 ChR2 expression allowed the photostimulation of cell bodies within the LPAG and the

248 selective activation of terminals from the LPAG that projected to the LC. An

249 optogenetic-assisted electrophysiological method was used to explore the connection

250 between LPAG^{Vglut2} and LC neurons (Fig. 5d, e)^{20, 21}. Compared to the baseline

251 condition, glutamate blockade with D-APV (25 μM) and NBQX (5 μM), along with

252 GABA receptor blockade (gabazine, 5 μM), reduced the mean values of

253 photostimulation and elicited spontaneous postsynaptic currents in the observed

254 LPAG^{Vglut2} neurons, while GABA receptor blockade did not induce any changes (Fig.

255 5d). When photostimulation was delivered to the LC, 65% of the recorded neurons in

256 the LC responded (Fig. 5e). The latency between photostimulation delivery and the

257 firing activity of the responding LC neurons is shown in Fig. 5f. It confirms that that

258 LC neurons receive glutamatergic inputs from the LPAG^{Vglut2} neurons. To identify the

259 cell types of the recorded LC neurons, biocytin was added to the recording

260 microelectrode solution for subsequent immunohistochemical staining for tyrosine

261 hydroxylase (TH), which is a marker of norepinephrine (NE) neurons. Then, we

262 confirmed that LPAG^{Vglut2} neurons mostly targeted TH-positive neurons in the LC (Fig.
263 5g). Optogenetic blue light activation of the LC at 30 Hz immediately induced
264 transitions from NREM sleep to wakefulness compared to yellow light (Fig. 5h, k). The
265 probability analysis of transition between each pair of sleep–wake stages indicated that
266 optical activation enhanced the probability to enter wakefulness, along with a
267 simultaneous reduction in the probabilities of the switch to NREM and REM sleep (Fig.
268 5i, j, l, m). Optogenetic blue light stimulation of the LC at 30 Hz led to a decrease in
269 EEG activity in the delta wave frequency range of 0–3.5 Hz, as well as an increase in
270 the theta wave frequency range of 4.5–7.25 Hz during wakefulness (Fig. 5n). Then, the
271 EMG_{Wake} was determined before and after blue light stimulation. Blue light
272 photostimulation significantly decreased the EMG_{Wake} level ($P = 0.0404$) (Fig. 5o). The
273 ratio of the EMG_{T-Wake} during wakefulness after treatment with photostimulation and
274 that the EMG_{N-Wake} during the normal wakefulness stage was significantly lower in the
275 blue light group than in the unstimulated normal counterparts ($P = 0.0365$) (Fig. 5p).
276 Importantly, photostimulation of LPAG^{Vglut2}-LC projections also promoted immobility
277 ($P = 0.0392$) (Fig. 5q). Additionally, chronic excitation of the LPAG^{Vglut2}-LC
278 projections for 1 h remarkably promoted long-term wakefulness and decreased NREM
279 and REM sleep in LPAG^{Vglut2}-ChR2 mice compared to the baseline controls (Fig. 5r–
280 u).

281 These results suggested a strong functional contribution of the LPAG^{Vglut2}-LC
282 projection in the induction of wakefulness and immobility.

283

284 **LPAG^{Vglut2} neurons induce arousal and immobility via the GiV pathway.**

285 Anterograde tracing results indicated that LPAG^{Vglut2} neurons project to the GiV, which
286 is important in regulating the sleep–wake cycle. To confirm the functional interaction
287 between the downstream target GiV and LPAG^{Vglut2} neurons, we used *in vivo* and *in*
288 *vitro* optogenetic approaches to activate the LPAG^{Vglut2}-GiV pathway. The AAV-DIO-
289 ChR2-mCherry construct was injected into the LPAG with optical fibers targeting the
290 axonal terminals in the GiV of Vglut2-Cre mice (Fig. 6a–c). Then, an optogenetic-
291 assisted electrophysiological experiment was conducted to determine the role of the
292 LPAG^{Vglut2} projection to the GiV neurons (Fig. 6d, e). Glutamate blockade with D-APV
293 (25 μ M) and NBQX (5 μ M), along with GABA receptor blockade (gabazine, 5 μ M),
294 decreased the mean values of activation and elicited spontaneous postsynaptic currents
295 in the recorded LPAG^{Vglut2} neurons compared to baseline; meanwhile GABA receptor
296 blockade did not induce any change compared to the baseline condition (Fig. 6d). A
297 total of 80% of recorded GiV neurons responded to the photostimulation (Fig. 6e). The
298 latency between photostimulation and the firing of the responding GiV neurons is
299 shown in Fig. 6f. Our results showed that the GiV neurons primarily receive
300 glutamatergic projections from the LPAG^{Vglut2} neurons. Then, we added biocytin to the
301 recording microelectrode solution for subsequent immunohistochemical staining for
302 Vglut2 and glycine and found that LPAG^{Vglut2} neurons targeted both Vglut2- and
303 glycine-positive neurons in the GiV (Fig. 6g).

304 Optogenetic blue light activation of the GiV at 30 Hz rapidly induced arousal from
305 NREM sleep compared to that using yellow light (Fig. 6h, k). Optical stimulation

306 increased the probability to induce wakefulness, along with a concomitant reduction in
307 the probability to switch to NREM and REM sleep (Fig. 6i, j, l, m). Optogenetic blue
308 light stimulation of the GiV at 30 Hz enhanced the activity in the frequency range of
309 4.25–5.75 Hz and reduction in the frequency range of 7–9.25 Hz of theta waves during
310 wakefulness (Fig. 6n). Blue light photostimulation of the LPAG^{Vglut2}-GiV pathway
311 significantly decreased the EMG_{Wake} level ($P = 0.0256$) (Fig. 6o). The ratio of the
312 EMG_{T-Wake} during wakefulness after treatment with photostimulation and that the
313 EMG_{N-Wake} during normal wakefulness was significantly lower in the blue light group
314 than in the unstimulated normal counterparts ($P = 0.0148$) (Fig. 6p). Furthermore,
315 photostimulation of the LPAG^{Vglut2}-GiV projections increased immobility ($P = 0.0068$)
316 (Fig. 6q). In contrast to LC stimulation, chronic stimulation of LPAG^{Vglut2}-GiV
317 projections for 1 h did not induce chronic wakefulness in LPAG^{Vglut2}-ChR2 mice (Fig.
318 6r–u).

319 The present data suggest that GiV is a crucial downstream nucleus for LPAG^{Vglut2}
320 neurons to generate wakefulness associated with immobility behavior.

321

322 **Chemogenetic inhibition of LPAG^{Vglut2} neurons inhibits REM sleep and promotes**

323 **NREM sleep.** To better understand the role of LPAG^{Vglut2} neurons in wakefulness and

324 REM sleep regulation, LPAG^{Vglut2} neurons were inhibited with AAV constructs that

325 encoded the engineered Gi-coupled hM4Di receptor (AAV-hSyn-DIO-hM4Di-

326 mCherry) in Vglut2-Cre mice (Fig. 7a, b). An *in vitro* study showed that CNO (5 μ M)

327 significantly reduced the number of evoked action potentials, frequencies, and

328 membrane potentials (Fig. 7c–e), while immunostaining demonstrated that CNO
329 administration suppressed c-Fos immunoreactivity in LPAG neurons expressing
330 mCherry in Vglut2 neurons (Fig. 7f–i). After CNO delivery, the sleep–wake states were
331 measured (Fig. 7j, k). The CNO-injected mice displayed decreased REM sleep and
332 enhanced NREM sleep compared to vehicle-injected mice. The amount of hourly REM
333 sleep was significantly reduced with CNO at 1 mg/kg by 31.12%, 28.57%, and 46.94%
334 during the second, third, and fourth hours, respectively, while the hourly duration of
335 NREM sleep after CNO treatment was increased by 13.82%, 25.78%, and 56.72%
336 during the second, third, and fifth hours, respectively. The hourly duration of
337 wakefulness after CNO injection was reduced by 30.39% and 18.10% during the third
338 and fifth hours, respectively (Fig. 7l). The duration of REM sleep during 15:00–19:00
339 was reduced by 35.57% ($P = 0.0067$), along with a 14.12% ($P = 0.0014$) increase in
340 NREM sleep and an 11.31% ($P = 0.0284$) reduction in wakefulness (Fig. 7m). CNO
341 injection did not induce any change in the EEG activity during REM sleep, NREM
342 sleep, or wakefulness (Fig. 7n). Chemogenetic inactivation of LPAG^{Vglut2} neurons did
343 not change the locomotor activity in the open field experiment ($P = 0.2663$) (Fig. 7o, p)
344 or increase immobility ($P = 0.4843$) (Fig. 7q). The EMG amplitude during REM sleep,
345 NREM sleep, and wakefulness were also evaluated after CNO treatment, but there was
346 no significant differences between the vehicle and CNO groups (Supplementary Figs.
347 3a–f). These findings indicate that the inhibition of LPAG^{Vglut2} neurons via hM4Di
348 decreases REM sleep and wakefulness, and increases NREM sleep, suggesting an
349 important role of LPAG^{Vglut2} neurons in the regulation of REM sleep and wakefulness,

350 without causing any changes in immobility.

351

352 **LPAG^{Vglut2} neurons activated during REM sleep projects to the SLD.** Using
353 combined optogenetic and neuroanatomical approaches, we explored the pathways by
354 which LPAG^{Vglut2} neurons regulate REM sleep. First, the AAV-DIO-ChR2-mCherry
355 construct was injected into the LPAG with AAV-DIO-eGFP targeting the SLD neurons
356 in Vglut2-Cre mice (Fig. 8a). Then, we used an optogenetic-assisted
357 electrophysiological approach to determine the properties of the projection between
358 LPAG^{Vglut2} and SLD neurons. Compared to the baseline condition, glutamate blockade
359 with D-APV (25 μ M) and NBQX (5 μ M), along with GABA receptor blockade
360 (gabazine, 5 μ M), reduced the mean values of photostimulation and induced
361 spontaneous postsynaptic currents in the observed LPAG^{Vglut2} neurons. However, the
362 GABA receptor blockade did not induce any changes (Fig. 8b). After photostimulation
363 delivery, 92.9% of the recorded neurons in the SLD responded (Fig. 8c). We summarize
364 the latency between the photostimulation delivery and the firing event in the responding
365 SLD neurons in Fig. 8d. These findings indicate that the SLD neurons mostly receive
366 glutamatergic inputs from LPAG^{Vglut2} neurons. By adding biocytin to the recording
367 microelectrode solution to enable subsequent immunostaining for Vglut2, we
368 confirmed that LPAG^{Vglut2} neurons mainly target Vglut2-positive neurons in the SLD
369 (Fig. 8e).

370 Since SLD is located adjacent to the LC, optogenetic stimulation of the LPAG-SLD
371 pathway might simultaneously induce the activation of the LPAG-LC projections.

372 Therefore, we used a neuroanatomical approach to elucidate the role of LPAG-SLD
373 projections in REM sleep regulation. By injecting a retrograde trace-cholera toxin b
374 subunit (CTb) into the SLD and GiV, we identified the neuronal pathways from the
375 LPAG activated during REM sleep (Fig. 8f). The CTb injection sites were restricted to
376 the SLD or GiV (Fig. 8g, h). To determine whether the LPAG-SLD and LPAG-GiV
377 pathways are activated during REM sleep, we used the flowerpot method for REM
378 sleep deprivation for 72 h, after which rats were allowed to recover for 2 h. Many c-
379 Fos+/CTb+ neurons were found in the LPAG of RSR rats after CTb injection into the
380 SLD (Fig. 8i, j). In contrast, after CTb injection into the GiV, only a few c-Fos+/CTb+
381 neurons were seldom found in the LPAG of RSR rats (Fig. 8k, l). Within the LPAG, the
382 number of c-Fos+/CTb+ neurons was 1.75 ± 0.22 in GiV-RSR rats and 7.35 ± 0.27 in
383 SLD-RSR rats ($P = 0.0050$) (Fig. 8m). Furthermore, we determined the percentage of
384 double-labeled neurons within the LPAG, and found that $28.37 \pm 4.24\%$ of CTb+
385 neurons were double-labeled in SLD-RSR rats compared to $9.57 \pm 1.68\%$ in GiV-RSR
386 rats ($P = 0.0060$) (Fig. 8m). These data suggest that the LPAG^{Vglut2}-SLD pathway, but
387 not the LPAG-GiV, is involved in the control of REM sleep.

388 **Discussion**

389 The LPAG is an important component of the periaqueductal gray and it regulates
390 several behaviors, including defensive behaviors, pain processing, chronic social defeat
391 stress, and sensorimotor responses to breathlessness^{22, 23, 24, 25}. These behaviors ensure
392 survival and rely on heightened arousal. In addition, the LPAG is connected to several
393 sleep–wake regulatory nuclei and has been observed to contain many c-Fos+ neurons
394 after REM sleep deprivation and rebound^{8, 18, 26}. In the present study, using fiber
395 photometry, chemogenetics, optogenetics, behavioral tests, polysomnography, and
396 electrophysiological experiments, we demonstrated a prominent contribution of
397 LPAG^{Vglut2} neurons to wakefulness associated with immobility and REM sleep, and we
398 determined the circuits involved (Supplementary Fig. 4).

399 Muscle tone, which is modulated across sleep–wake states, is maximized during
400 wakefulness, reduced during NREM sleep, and absent during REM sleep^{27, 28}. However,
401 chemogenetic and optogenetic activation of the LPAG^{Vglut2} neurons in our study
402 induced wakefulness with immobility. The excitation of the LPAG^{Vglut2} neurons also
403 induced an increase in the EEG power of theta waves, which depend on the
404 hippocampus²⁹. We propose that the dominant effect of the induction of wakefulness,
405 covered up the REM sleep-promoting effects of LPAG^{Vglut2} neurons. Indeed, REM
406 sleep is decreased and NREM sleep is increased when all LPAG^{Vglut2} neurons are
407 inhibited, indicating that two population of LPAG^{Vglut2} neurons are co-distributed and
408 play roles in wakefulness or REM sleep. These neurons could be candidate targets for
409 the treatment of sleep disorders, including REM sleep behavior disorder and narcolepsy.

410 The immobility behavior reported in our study could correspond to the classical
411 defense-related immobile state named freezing. Indeed, freezing mainly refers to the
412 absence of physical movement as reflected on EMG recording and automated scoring
413 of video recording³⁰. We did not define the immobility behavior in our present study as
414 freezing, because freezing is a defensive state of immobility characterized by the
415 cessation of all movements accompanied by the parasympathetic-induced heart rate
416 deceleration (i.e., bradycardia)³¹ and we cannot determine with our analysis whether
417 the immobility induced correspond to a freezing. We did not monitor the heart rate and
418 other parameters of mice during chemogenetic or optogenetic manipulation. In addition,
419 despite being immobilized, the muscle tone is high during freezing, which is not in line
420 with the low muscle tone intensity observed in our study. Furthermore, general
421 immobility can be identified as an absence of movements, whereas a sleep state is also
422 seen as a state of immobility. The EMG of neck muscle recording is useful to
423 discriminate the defense-related immobility from sleep³². In our study, the EMG
424 amplitude during the stimulation was less than that in spontaneous wakefulness and we
425 therefore defined it as a state of immobility.

426 Our study showed that LPAG^{Vglut2} neurons project to different several brain regions.
427 We further showed that the LPAG^{Vglut2} neurons promote arousal and immobility via the
428 LC^{NE} connections. These results are consistent with those of previous studies, which
429 showed that LC received a strong projection from PAG^{33, 34}. LC is the most dorsal of
430 the ten noradrenergic nuclei located in the pontine brainstem³⁵. These LC^{NE} neurons are
431 critical to induce wakefulness^{36, 37, 38}. In the state of wakefulness, tonic LC^{NE} activity

432 correlates with the state and covaries with the levels of arousal³⁹. In addition to tonic
433 discharge rates, LC^{NE} neurons generate phasic bursts when exposed to novel or
434 significant stimuli⁴⁰. An increased EEG frequency, as well as behavioral markers of
435 attention and alertness, reflect the phasic LC activity⁴⁰. Furthermore, LC neurons
436 exhibit vigilant state-dependent changes in their firing properties: they are highly active
437 during wakefulness, they are much less active during NREM sleep, and they are almost
438 silent during REM sleep^{41, 42}. Deactivated LC neurons may promote NREM and REM
439 sleep, while activated neurons in the LC may participate in the maintenance of
440 wakefulness^{36, 43}. LC^{NE} neurons projecting to the lateral amygdala receive synaptic
441 input from orexin neurons in the lateral hypothalamus, which plays an important role
442 in the regulation of passive defensive behaviors⁴⁴. Combined with previous findings,
443 our data provide an enhanced understanding of the roles of LPAG^{Vglut2}-LC^{NE} neurons
444 in the sleep–wake cycle. They also suggest that these neurons increase arousal while
445 ensuring the expression of an appropriate behavioral response. This study suggests that
446 the pathway involved in fear generalization is the one that is sometimes seen in
447 conditions such as posttraumatic stress disorder.

448 Another projection from LPAG^{Vglut2} to GiV^{vglut2/glycine} neurons is responsible for the
449 effects on the initiation of wakefulness and immobility. GiV is also known as the
450 magnocellular reticular nucleus located in the ventromedial medullary reticular
451 formation⁴⁵. The glycinergic premotoneurons in the GiV are REM-on neurons, and the
452 descending REM-on glutamatergic neurons in the SLD induce muscle atonia through
453 their excitatory projections to the GiV^{glycine} inhibitory neurons^{46, 47, 48}. Optogenetic

454 activation of glutamatergic neurons in the ventral medulla, which mainly includes Giv,
455 induces wakefulness⁴⁹. Furthermore, GiV is involved in motor control and this region
456 also receives projections from VLPAG neurons to induce passive defensive behaviors⁵⁰.
457 Our results showed that the LPAG^{Vglut2} neurons project to the GiV neurons expressing
458 either glycine or Vglut2, and the optogenetic activation of GiV neurons initiated
459 wakefulness, without maintaining the state, owing to the dual effects of these two
460 neuron types. LPAG^{Vglut2} neurons may have initiated wakefulness via the projection to
461 GiV glutamatergic neurons, while they promoted immobility with low muscle tone
462 intensity similar to the muscle atonia during REM sleep through the GiV^{glycine} inhibitory
463 neurons.

464 We also found that LPAG^{Vglut2} neurons are also involved in REM sleep regulation.
465 Trap and c-Fos staining experiments demonstrated the role of LPAG^{Vglut2} neurons in
466 the regulation of REM sleep. Chemogenetic inhibition of LPAG^{Vglut2} neurons decreased
467 REM sleep, although chemogenetic and optogenetic activation of these neurons
468 promoted wakefulness, likely masking the effect on REM sleep. Projections to the SLD
469 derived from the LPAG^{Vglut2} neurons are likely responsible for REM sleep onset and
470 maintenance. There is an anatomical connection between the LPAG and SLD and GiV⁵¹.
471 Both the glutamatergic neurons in the SLD and glycinergic neurons in Giv are crucial
472 REM-on neurons. The activation of REM-on glutamatergic neurons from the SLD
473 initiates and maintains REM sleep. Descending REM-on glutamatergic SLD neurons
474 induce muscle atonia via their excitatory projections to the glycinergic premotoneurons
475 located in the GiV⁵¹. When we injected CTb in the SLD and GiV, we confirmed the

476 existence of a strong LPAG-SLD pathway but only a weak LPAG-GiV pathway
477 activated during REM sleep rebound. Hence, it seems that the LPAG–SLD pathway,
478 but not the LPAG–GiV pathway, is likely involved in the induction of REM sleep by
479 LPAG^{Vglut2} neurons.

480 In our present study, we found that mostly different neurons in the LPAG were
481 activated during wakefulness and REM sleep in the TRAP mice. Therefore, two
482 different populations of glutamatergic neurons are active during wakefulness and REM
483 sleep in the LPAG. In future studies, these two different subpopulations should be
484 studied separately by means of the discovery of specific markers and the use of Cre
485 mice.

486 In conclusion, we found that LPAG^{Vglut2} neurons are essential for controlling the
487 wakefulness associated with immobility via the LC and GiV pathways. Another
488 population of LPAG^{Vglut2} projecting to the SLD would regulate REM sleep. Our results
489 suggested that LPAG^{Vglut2} neurons constitute a potential therapeutic target for the
490 treatment of neuropsychiatric disorders with sleep–wake abnormalities.

491

492 **Methods**

493 **Animals.** Vglut2-Cre transgenic mice (males, 22–26 g) obtained from Jackson
494 Laboratory (Bar Harbor, ME, USA) and Sprague Dawley rats (males, 240-280 g)
495 obtained from Charles River Laboratories (Wilmington, MA, USA) were placed
496 separately in Plexiglas cylinders with an outer diameter of 30 cm and a height of 40 cm.
497 The Fos^{2A-iCreER/+} transgenic mice (TRAP2) for activity-dependent genetic labeling
498 were kindly provided by Dr Li-Qun Luo from Stanford University and crossed with
499 R26^{Ai14/+} mice (Ai14) to produce double heterozygous (TRAP2; Ai14, TRAP-RED)
500 mice^{52,53} (Supplementary Fig. 1a). The animals were housed at a temperature of 22 °C,
501 humidity of 60%, and illumination of 100 lux under a 12/12 h light/dark cycle (lights
502 on: 07:00). Food and water were provided ad libitum. Animal care and experiments
503 were performed in accordance with the institutional guidelines and regulations of
504 Chinese and European governments. The experimental protocols were approved by the
505 Animal Care and Use Committee of Fudan University, China and the University of
506 Lyon 1, France.

507

508 **Chemicals and drug administration.** CNO (C0832, Sigma-Aldrich, St. Louis, MO,
509 USA) saline solution (0.1 mg/ml) was used for the *in vivo* experiments, and the volume
510 was determined by body weight (10 ml/kg). For *in vitro* experiments, a stock CNO
511 solution was produced using artificial cerebral spinal fluid (ACSF) and diluted to 5 μM.
512 A stock 4-OHT (H6278, Sigma-Aldrich) ethanol solution (20 mg/ml) was produced by
513 adding the correct quantity of ethanol, and putting it onto a vortex mixer, followed by

514 a shaker at 37°C for 15 min or until completely dissolved. An aluminum foil was used
515 to minimize the exposure to light. A working solution (10 mg/ml) was prepared by
516 adding corn oil (C8267, Sigma-Aldrich) to the stock solution and allowing the ethanol
517 to evaporate using a speed-vac for 2–3 hr. The drug was administered intraperitoneally
518 depending on the time (Supplementary Fig. 1a).

519

520 **Viral injections and fiber implantations.** The viruses were packaged into the AAV
521 serotype 2/9 vectors with titers of almost $1-5 \times 10^{12}$ genomic copies/mL. AAV-EF1 α -
522 DIO-GCaMP6f, AAV-hSyn-DIO-hM3Dq/hM4Di-mCherry, AAV-EF1 α -DIO-ChR2-
523 mCherry, and AAV-lox-stop-hrGFP were purchased from Shanghai Taitool Inc.
524 (Shanghai, China) or BrainVTA, Co., Ltd. (Wuhan, China).

525 Mice were anesthetized with pentobarbital sodium (50 mg/kg, i.p.) and placed onto
526 a stereotaxic apparatus (RWD Life Science, Shenzhen, China). A midline scalp incision
527 was made to expose the skull followed by unilateral or bilateral craniotomy directly
528 above LPAG (AP: – 4.1 mm, ML: \pm 0.35 mm, DV: – 2.3 mm). Then a glass pipette was
529 carefully lowered into the LPAG for virus microinjection using a compressed air system
530 and nitrogen gas with 20–40 psi pulses. After the injection was administered, the glass
531 pipette was held in place for 10 min, allowing the virus to diffuse. The animals were
532 placed on a heated surface until they fully recovered from anesthesia, then, the mice
533 were returned to their home cage.

534 For the fiber photometry recording, Vglut2-Cre mice were microinjected with AAV-
535 EF1 α -DIO-GCaMP6f into the left side of the LPAG at a volume of 30 nL. After the

536 injection, a ceramic ferrule and optic fiber assembly (inner diameter: 200 μm , numerical
537 aperture (NA): 0.37; Newdoon, Shanghai, China) was implanted using the following
538 coordinates (AP: -4.1 mm, ML: ± 0.35 mm, DV: -2.2 mm) such that the fiber tip was
539 located on top of the left LPAG. To activate or inhibit the LPAG^{Vglut2} neurons with
540 DREADDs, Vglut2-Cre mice 30 nL of either AAV-hSyn-DIO-hM3Dq-mCherry or
541 AAV-hSyn-DIO-hM4Di-mCherry on both sides of the LPAG. For the activation of the
542 LPAG^{Vglut2} neurons and their pathways with optogenetics, 30 nL of AAV-EF1 α -DIO-
543 ChR2-mCherry was bilaterally microinjected into the LPAG in Vglut2-Cre mice. Then
544 the mice were unilaterally implanted with optical fibers (inner diameter: 200 μm , NA:
545 0.37; Newdoon) above the LPAG (AP: -4.1 mm, ML: ± 0.35 mm, DV: -2.2 mm), LC
546 (AP: -5.4 mm, ML: ± 0.8 mm, DV: -3.7 mm), or GiV (AP: -6.7 mm, ML: ± 0.3 mm,
547 DV: -4.3 mm). To explore the output patterns of the LPAG^{Vglut2} neurons, Vglut2-Cre
548 mice were unilaterally microinjected with 200 nL of AAV-lox-stop-hrGFP in the LPAG.

549 Mice were allowed to rest for at least 3 weeks to recover completely after being
550 injected with the virus and allow viral expression before further experiments. In all
551 experiments, the animals with incorrect injection sites were excluded from further
552 analyses.

553

554 **EEG/EMG electrode implantation surgery.** EEG recordings and analysis were
555 performed as previously described^{54, 55, 56}. Under pentobarbital sodium anesthesia (50
556 mg/kg, i.p.), two stainless steel screws attached to a Teflon-coated stainless-steel wire
557 (1 mm diameter) were inserted through the skull into the cortex and served as EEG

558 electrodes; two Teflon-coated stainless-steel wires were placed bilaterally into the
559 trapezius muscles and served as EMG electrodes. All wires were attached to a micro-
560 connector as well as to the skull with dental cement.

561 Male Sprague-Dawley rats were implanted with EEG and EMG electrodes under
562 anesthesia with ketamine (Virbac Santé Animale, Carros, France; 100 mg/kg, i.p.) and
563 xylazine (Bayer, 50 mg/kg, i.p.). Lidocaine (Xylovet, Ceva Santé Animale, Libourne,
564 France) was subcutaneously injected for analgesia. Three stainless steel screws were
565 fixed in the parietal and frontal bones, and a unipolar EEG recording was fixed on the
566 cerebellum bone. Two wire electrodes were inserted into the neck muscles for bipolar
567 EMG recordings. All leads were connected to a miniature plug (Plastics One Inc.,
568 Torrington, CT, USA), which was glued to the skull.

569

570 **Polygraphic recordings and analysis.** Cortical EEG and neck EMG signals were
571 amplified, filtered (Biotex, Kyoto, Japan; EEG, 0.5–30 Hz; EMG, 20–200 Hz) and
572 digitized at a sampling rate of 128 Hz using VitalRecorder (Biotex). Using a standard
573 algorithm, sleep-wake stages were categorized offline into 4-second epochs of
574 wakefulness, NREM or REM sleep by SleepSign (Biotex). Then, the epochs were
575 visually examined and corrected if necessary. EEG power density was calculated using
576 fast Fourier transform with a 0.25 Hz resolution, and presented as a percentage of the
577 total power across 0–25 Hz. Based on the protocols of previous studies⁵⁷, we used the
578 original EMG data and mean values from SleepSign (Biotex) recordings to quantify the
579 nuchal muscle tone. For chemogenetic activation manipulation, we analyzed the muscle

580 tone during 10:00–13:00 after administration of vehicle or CNO. For optogenetic
581 inactivation manipulation, we analyzed the muscle tone during 60-s stimulation or
582 interval period, eliminating the first and last 4 seconds to avoid the change in muscle
583 tone caused by the transition of the vigilance stage. To reduce the individual differences
584 in mice, the mean EMG values were normalized by baseline mean EMG value^{48, 58}. To
585 avoid muscle tone alterations induced by the transition of the vigilance stage, we only
586 included the wakefulness episodes that lasted for more than 48 s and excluded the first
587 and last 8 seconds in the quantification process.

588 After the surgery, rats were allowed 1 week of recovery in the Plexiglas cylinder.
589 Then, a cable was connected to the plug on the rats with the other end attached to a slip-
590 ring commutator to allow free movement of the rats in the cylinder. Another 3 days of
591 habituation were allowed before data collection. EEG and EMG signals were digitized
592 through a CED interface using Spike2 software (Cambridge Electronic Design,
593 Cambridge, UK). Vigilance stages were categorized accordingly.

594

595 **Protocols for REM sleep deprivation and rebound.** In the TRAP experiment, REM
596 sleep deprivation was performed using an automated method involving the online
597 signal analysis software Sleepscore^{59, 60} (Viewpoint, New South Wales, Australia). The
598 vigilance state was automatically labeled for each 1-s epoch based on several
599 discriminant parameters of EEG/EMG signals. When a REM sleep episode was
600 detected, a signal was transmitted to a stimulation box through Matlab, and the animal
601 was awakened by vertical shaking of the cylinder floor via an electromagnet^{61, 62}. The

602 48-hour automatic REM sleep deprivation was highly efficient in mice with only 2.2%
603 of remnant REM sleep⁵⁹. REM sleep deprivation started at 10:00, when the proportion
604 of REM sleep was high. After 48 h of REM sleep deprivation, mice were returned to
605 their home cylinder and allowed to sleep *ad libitum* during a 2-h recovery period
606 (Supplementary Fig. 1a). RSR-RSR animals were injected with 4-OHT after 2 h of RSR.
607 One week later, the animals were subjected to REM sleep deprivation and perfused after
608 2 h of RSR. In W-RSR or W-W animals, mice were placed in a white open-field box
609 (base, 45 × 45 cm) containing several toys for 2 h. The animals were monitored using
610 video and polysomnography. Whenever the mice fell asleep, they were awakened by
611 slow repositioning of the toys or the gentle touch of a soft tissue. One week later, W-W
612 animals underwent the same procedure, whereas the W-RSR animals were deprived of
613 REM sleep for 48 h and allowed to recover for 2 h before perfusion.

614 REM sleep deprivation was performed using the flowerpot method⁶³. Rats were
615 divided into three groups: control, REM sleep deprivation for 3 days, and recovery after
616 REM sleep deprivation for 3 days. Animals in the control group were kept in the
617 standard cage throughout the experiment. At 12:00 A.M., REM sleep deprived rats were
618 placed in a Plexiglas cylinder containing three platforms (6.2 cm diameter, 7–12 cm
619 height), which were surrounded by water (2 cm) for 75 h. Rats with REM sleep rebound
620 syndrome received the same treatment for 72 h, and were allowed to recover in a
621 cylinder with a dry bed of woodchips. They were euthanized 2 h after the first REM
622 sleep episode. During the periods of deprivation, food and water were available *ad*
623 *libitum*, and cylinders were cleaned daily.

624

625 **Fiber photometry.** The calcium transients of Vglut2 neuronal cell bodies in the LPAG
626 of freely moving mice were recorded by optical fiber photometry as previously
627 described. In short, to induce fluorescent signals, a 488-nm laser (OBIS 488LS,
628 Coherent Inc., Santa Clara, CA, USA) beam was reflected from a dichroic mirror
629 (MD498, Thorlabs Inc, Newton, NJ, USA), focused by an objective lens (Olympus,
630 Tokyo, Japan), and coupled through a fiber collimation package (F240FC-A, Thorlabs
631 Inc) into a patch cable which was connected to the ferrule of an upright optical fiber
632 implanted in the mouse via a ceramic sleeve (125 μm O.D.; Newdoon). GCaMP6
633 fluorescence was bandpass filtered (MF525–39, Thorlabs Inc, New Jersey, USA) and
634 collected by a photomultiplier tube (R3896, Hamamatsu, Higashi-ku, Hamamatsu City,
635 Shizuoka, Japan). An amplifier (C7319, Hamamatsu) was used to convert the current
636 output from the photomultiplier tube into voltage signals, which was further filtered
637 through a low-pass filter (40-Hz cut-off; Brownlee 440, Santa Clara, CA, USA). The
638 photometry voltage traces were downsampled to match the EEG/EMG sampling rates
639 using a Power 1401 digitizer and Spike2 software (Cambridge Electronic Design).
640 Photometry data were exported as Matlab mat files from the Spike 2 software for further
641 analysis. The value of the photometry signal ($\Delta F/F$) was calculated as $(F-F_0)/F_0$, where
642 F_0 is the mean fluorescent signal. The average $\Delta F/F$ values were calculated for all
643 sleep–wake states. To analyze the state transitions, we identified each state transition
644 and aligned $\Delta F/F$ in a ± 50 -s window around each point that was calculated. The
645 average peak of the $\Delta F/F$ in different sleep stages was compared^{64, 65}.

646

647 **Optogenetic manipulations during polygraphic recordings.** For *in vivo* light
648 manipulations, light pulses were generated by a laser stimulator (SEN-7103, Nihon
649 Kohden, Tokyo, Japan) and output through an isolator (ss-102J, Nihon Kohden). A
650 rotating optical joint (FRJ_FC-FC, Doric Lenses, Quebec, Canada) was used to reduce
651 the torque on the implant on animals and attached to one end of the optical fiber. Light-
652 pulse trains (5-ms duration each) were programmed and carried out during the light
653 period, when mice were inactive. Chronic photostimulation lasted for 1 h, with 5-ms
654 pulses at 30 Hz followed by rest for 20 s after every 40 s (60 cycles). EEG/EMG
655 recordings during the same period of the previous day served as control. The parameters
656 of the sleep–wake cycle were analyzed. Power intensities of blue or yellow light at the
657 optical fiber tip were measured using a power meter (PM10, Coherent) and calibrated
658 to 3–7 mW.

659

660 **Behavioral tests.** The open field test (OFT) is commonly used to test locomotor activity
661 in mice⁶⁶. In a quiet and sound-proof room with dim light (≈ 20 lux), individual mice
662 were placed in a 50 × 50-cm arena with black surface and enclosed by 40 cm high walls
663 and were allowed to move freely for 15 min. The activities of the test subjects were
664 recorded using an automatic video tracking system (Labmaze V3.0, Beijing Zhongshi
665 Dichuang Technology Development Co., Ltd., Beijing, China). The OFT was
666 performed 30 min after CNO or vehicle treatment. After each trial, the instrument was
667 wiped clean with a 75% alcohol solution to remove traces left by the previous mouse.

668 Rearing was defined by the mouse lifting both of its forelimbs off the floor. When
669 rearing happened along the walls of the arena, the mouse typically leaned against the
670 walls.

671 For chemogenetic and optogenetic manipulation, the immobility time was recorded
672 by a video camera positioned on the front side of the recording chambers. The data were
673 analyzed using Labmaze V3.0 software (Beijing Zhongshi Dichuang Technology
674 Development Co., Ltd) at a 5% immobility threshold^{67, 68}.

675

676 **Histological procedures.** Under deep anesthesia, the animals were transcardially
677 perfused with 4% paraformaldehyde. Brains were removed, post-fixed and dehydrated
678 in 30% graded phosphate-buffered sucrose solution. Then, the brains were coronally
679 sliced into 30- μ m sections on a cryostat. For *in situ* hybridization experiments,
680 continuous floating sections were collected in RNase-free cryoprotectant solution and
681 stored at -20°C for use. As previously mentioned, the free-floating sections were
682 stained by immunohistochemistry. In brief, brain sections were rinsed in PBS,
683 incubated at room temperature in 0.3% hydrogen peroxide in PBS (0.1 M) for 30 min,
684 and incubated at room temperature for 1 h in 3% normal donkey serum and 0.3% Triton
685 X-100 in PBS (PBST). The primary antibody, which was rabbit anti-c-Fos (1:10000;
686 Millipore, Darmstadt, Germany), was double stained, diluted in PBST, and reacted with
687 brain slices overnight at 4°C . On the next day, the sections were rinsed in PBS and
688 incubated for 2 h in biotinylated anti-rabbit secondary antiserum (1:1000; Jackson
689 ImmunoResearch, Laboratories, West Grove, PA, USA). The brain slices were coated

690 with the avidin-biotin-peroxidase complex (1:1000; Vector Laboratories, Burlingame,
691 CA, USA) for 1 h. The immunoreactive cells were promoted through the reaction with
692 0.04% diaminobenzidine tetrahydrochloride and 0.01% hydrogen peroxide which was
693 enhanced by nickel. This procedure was conducted on the same section to detect the
694 expression of mCherry, which used the rat anti-mCherry (1:10000; CLONTECH
695 Laboratories, Inc., Palo Alto, CA, USA) as the primary antibody and anti-rat secondary
696 antiserum without nickel for the visualization. Finally, the brain sections were mounted
697 on glass slides and observed under the microscope (Olympus BX51, Tokyo, Japan). A
698 digital camera (DP72, Olympus) captured the images.

699 In the c-Fos immunohistochemistry combined with Vglut2 *in situ* hybridization
700 experiments, the recombinant plasmid (pCRII-TOPO, Invitrogen, Carlsbad, CA, USA)
701 containing the Vglut2 cDNA was linearized by Not I and Hind III (New England
702 Biolabs, Ipswich, MA, USA), and transcribed using SP6 and T7 RNA polymerases (for
703 antisense and sense riboprobes, respectively). A non-radioactive RNA labeling kit
704 (Roche Diagnostic, Rotkreuz, Switzerland) was used for the transcription of riboprobes
705 according to the manufacturer's instructions. The digoxigenin-labeled riboprobes were
706 stored in a hybridization buffer at -20 °C. As described previously^{55, 69}, brain sections
707 were incubated for 18 h with a rabbit antiserum to c-Fos (1:3000 for Vglut2, Merck,
708 Darmstadt, Germany) in PBST at room temperature. Then, the brain sections were
709 successively incubated at room temperature with a biotinylated goat antirabbit IgG
710 solution (1:1000, Vector Laboratories) and an ABC-HRP solution (1:1000, Elite kit,
711 Vector Laboratories) both for 90 min each. These sections were submerged for almost

712 15 min in a 0.05 M Tris-HCl buffer, which contained 0.025% 3,3-diaminobenzidine-4
713 HCl (DAB, Sigma-Aldrich) and 0.003% H₂O₂. Brain sections were rinsed for three
714 times in PBST between steps and incubated in PBST containing 10 mM dithio-threitol
715 (DTT, Sigma-Aldrich) twice for 10 min and in a standard saline citrate solution (SSC
716 2X) for 10 min. All buffers except DTT contained 0.2% RNase inhibitor (Sigma-
717 Aldrich). Brain sections were subjected to the hybridization buffer consisting of 150
718 mM NaCl, 8 mM Tris-HCl, 1 mM Tris-Base, 6 mM NaH₂PO₄, 5 mM Na₂HPO₄, 5 mM
719 EDTA, 50% formamide, 10% dextran sulphate, yeast tRNA (Sigma type III, 1 mg/mL,
720 Sigma-Aldrich), 0.02% ficoll, and 0.02% polyvinyl pyrrolidone-containing 0.5 g/mL
721 of the digoxigenin-labeled probe overnight at 65°C. Sections were rinsed twice at 55°C
722 for 20 min in the complex of SSC 1X, 50 % formamide and 0.1 % Tween-20. Then, the
723 sections were treated at 37°C for 15 min with 10 µg/µl RNase A in Tris 10 mM-
724 containing 1 mM EDTA and 500 mM NaCl. After rinsing with PBST three times,
725 sections were incubated overnight with an anti-digoxigenin antibody conjugated to
726 alkaline phosphatase (1:2000, Roche Diagnostic) in PBST containing 0.2% blocking
727 agent (Roche Diagnostic). Then, they were rinsed twice in PBST, once in PBS 10 mM,
728 and once in a buffer containing 1 M Tris-HCl, 1 M NaCl, 500 mM MgCl₂, and 1%
729 Tween-20. Each wash lasted 10 min. Sections were then incubated at 37°C in the same
730 buffer containing nitroblue tetrazolium and 5-bromo-4-chloro-3-indolyl-phosphate (20
731 µl/mL, Roche Diagnostic). After 4 h of incubation in the revelation buffer, sections
732 were washed in PBST twice for 10 min each. Finally, the sections were mounted on
733 glass slides, dried, and covered with Vectamount (Vector Laboratories). In the absence

734 of primary antibodies (anti-c-Fos and anti-digoxigenin) or with the sense probe, the
735 control group ensured the labeling specificity^{19,48}.

736

737 **Immunostaining analysis.** The atlas of Swanson served as a reference for the
738 structures (Swanson 1992). Double- or single-labeled sections were drawn using an
739 Axioscope microscope (Zeiss, Oberkochen, Germany), equipped with a motorized X-
740 Y-sensitive stage and a video camera, which was connected to a computerized image
741 analysis system (Mercator, Explora Nova, La Rochelle, France). On both sections (-5.6
742 and -8.6 mm to Bregma), the number of double-labeled Fos-Vglut2 neurons was
743 quantified at the LPAG level, and ImageJ software (National Institutes of Health,
744 Bethesda, MD, USA) was used to measure optical density^{18,19}.

745

746 ***In-vitro* electrophysiology.** The brain slices (280- μ m coronal sections) from male
747 Vglut2-Cre mice were prepared with a vibratome (VT-1200, Leica Microsystems,
748 Wetzlar, Germany) under general anesthesia. Almost 25 ml of ice-cold (4 °C)
749 oxygenated cutting solution was perfused in a Vglut2-Cre mouse who developed
750 unconsciousness, followed by decollation as soon as possible. The mouse brain was
751 carefully and rapidly removed and placed into ice-cold oxygenated cutting solution,
752 trimmed, translated, and fixed on an ice-cold plate infiltrated with ice-cold oxygenated
753 cutting solution. The slices included four brain regions: the LPAG, LC, GiV, and SLD.
754 The ingredients of the cutting solution (a) and ACSF (b) included the following: (a) 213
755 mM sucrose, 10 mM glucose, 2.5 mM KCl, 1.25 mM NaH₂PO₄, 26 mM NaHCO₃, 3

756 mM MgSO₄, 0.1 mM CaCl₂ and 0.4 mM Ascorbic Acid, at 4 °C. (b) 25 mM glucose,
757 119 mM NaCl, 2.5 mM KCl, 1.25 mM NaH₂PO₄, 26 mM NaHCO₃, 1 mM MgCl₂ and
758 2 mM CaCl₂, at 32 °C. Brain sections were incubated in ACSF at 32 °C for the first 30
759 min and then shifted to room temperature for the next 30 min. Notably, the solutions
760 used for the experiments were fresh and contained 95% O₂ and 5% CO₂. The electrodes
761 were backfilled with the internal potassium gluconate solution to record the
762 electrophysiological activity of the targeted neurons. These electrodes had a resistance
763 range of 4–7 MΩ. The potassium gluconate internal solution (c) contained the following:
764 (c) 130 mM K-gluconate, 10 mM Hepes, 10 mM KCl, 0.5 mM EGTA, 4 mM ATP-Mg,
765 0.5 mM GTP-Na, and 10 mM phosphocreatine (pH = 7.5). Short-term (50 ms) injected
766 currents (20 pA) were used to test the input resistance. All electrodes used in the
767 experiments were backfilled with the internal solution of potassium gluconate.

768 For whole-cell patch-clamp recording, the slices were placed into the recording
769 chamber filled with oxygenated ACSF (liquid dropped at 1–2 ml/min). Using infrared
770 differential interference contrast and a fluorescence microscope, the neurons with good
771 shape and specific fluorescence were targeted. The current-clamp and voltage-clamp
772 recording modes were used to record the voltage (mV) and currents (pA), respectively.
773 For the *in vitro* optogenetic experiments, the AAV-hSyn-DIO-ChR2-mCherry virus was
774 microinjected into the LPAG of the Vglut2-Cre male mice. The virus required at least
775 3 weeks to affect the somas and fibers of the LPAG^{Vglut2} neurons. Then, we tested the
776 activity of the affected LPAG^{Vglut2} neurons with 473-nm light in the designed protocols,
777 including the electrophysiological properties and fidelity. To verify the feasibility of the

778 neural pathway from the LPAG to the LC, GiV or SLD, 473-nm light was applied onto
779 the LPAG^{Vglut2} fibers in the LC, GiV or SLD, respectively, which was confirmed by the
780 existence of postsynaptic currents after optogenetic activation. To identify the neural
781 origin of LPAG^{Vglut2} inputs, the postsynaptic currents recorded from the projected
782 neurons were perfused sequentially with ACSF, gabazine (SR, 5 μ M), 2-amino-5-
783 phosphonopentanoic acid (D-APV, 25 μ M), and 2,3-dihydroxy-6-nitro-7-sulfamoyl-
784 benzo[f]quinoxaline-2,3-dione (NBQX, 5 μ M). Note that the inhibitory postsynaptic
785 currents (IPSCs) were blocked by gabazine to demonstrate the differences in excitatory
786 postsynaptic currents (EPSCs), while D-APV and NBQX were applied to block the
787 glutamatergic currents (or EPSCs) induced by AMPA and NMDA receptors to illustrate
788 the influence on IPSCs. All drugs were diluted with ACSF. Data were acquired, filtered
789 (low-pass filtered at 1 kHz), and digitized (at 4 kHz) in the recording system using p-
790 Clamp 10.3 software (Axon Ins., Washington, DC, USA), Multi-Clamp 700B Amplifier
791 (Axon Ins.) and Micro1401 (CED Ins., Cambridge, UK). Neurons with Ra of over 30
792 M Ω or a floating range over 20% were excluded. To record the morphological data
793 from mice, the solution containing biocytin was selected. The brain slices with the
794 recorded neurons were post-fixed overnight after whole-cell recording. The brain slices
795 were rinsed with 0.01 M PBS 3–5 times, and then incubated with streptavidin in 0.01
796 M PBST (1:1000) at 4 $^{\circ}$ C for 12 h. Then the sections were rinsed with 0.01 M PBS 3–
797 5 times at room temperature and incubated with other antibodies if other labeling was
798 needed. Finally, the antifade solution was applied. Fluorescence images were obtained
799 using an Olympus IX71 microscope or a Leica confocal system^{20, 69}.

800

801 **Statistical analysis.** Data are expressed as mean \pm standard error of the mean (SEM).

802 Two-way repeated-measures analysis of variance (ANOVA) was used to compare

803 multiple data between the groups. Paired and unpaired *t*-tests were used for single-value

804 comparisons. One-way ANOVA was used to compare more than two groups, and the

805 *post-hoc* Tukey test was applied for multiple pairwise comparisons. A two-tailed *p*-

806 value < 0.05 was considered statistically significant. We used SPSS software (version

807 16.0; IBM, Corp., Armonk, NY, USA) for data analysis.

808

809 **Data availability**

810 The data that support the findings of this study are available from the corresponding

811 authors upon reasonable request.

812

813 **Code availability**

814 The custom-written analysis code is available from the corresponding author upon

815 reasonable request.

816

817 **Acknowledgements**

818 We thank Dr. Wen-Ying Liu and Dr. Dian-Ru Wang for technical assistance in *in-vitro*
819 electrophysiological and neuroanatomical experiments. This study was supported by
820 the National Major Project of China Science and Technology Innovation 2030 for Brain
821 Science and Brain-Inspired Technology (2021ZD0203400 to Z.-L.H.), the National
822 Natural Science Foundation of China (82171479, 81871037 to Y.-Q. W.; 82020108014
823 and 32070984 to Z.-L.H.), the Shanghai Science and Technology Innovation Action
824 Plan Laboratory Animal Research Project (201409001800 to Z.-L.H.), Program for
825 Shanghai Outstanding Academic Leaders (to Z.-L.H.), the Shanghai Municipal Science
826 and Technology Major Project, and ZJLab (2018SHZDZX01 to Z.-L.H.).

827 **Author contributions**

828 Z.L.H, P.L. and Y.Q.W conceived the study. L.L., Y.Q.W., and S.A. performed the
829 behavioral experiments. L.L., and Y.Q.W. performed the anatomical experiments. J.B.J.
830 performed the electrophysiological experiments. Y.Q.W, L.L., P.L. and Z.L.H. wrote
831 the paper.

832 **Competing interests**

833 The authors declare no competing interests.

834

835

836 **References**

- 837 1. Koolhaas JM, *et al.* Coping styles in animals: current status in behavior and stress-
838 physiology. *Neurosci Biobehav Rev* **23**, 925-935 (1999).
839
- 840 2. LeDoux J. Rethinking the emotional brain. *Neuron* **73**, 653-676 (2012).
841
- 842 3. Koutsikou S, Apps R, Lumb BM. Top down control of spinal sensorimotor circuits essential
843 for survival. *J Physiol* **595**, 4151-4158 (2017).
844
- 845 4. Kozłowska K, Walker P, McLean L, Carrive P. Fear and the Defense Cascade: Clinical
846 Implications and Management. *Harv Rev Psychiatry* **23**, 263-287 (2015).
847
- 848 5. Borelli KG, Nobre MJ, Brandao ML, Coimbra NC. Effects of acute and chronic fluoxetine
849 and diazepam on freezing behavior induced by electrical stimulation of dorsolateral and
850 lateral columns of the periaqueductal gray matter. *Pharmacol Biochem Behav* **77**, 557-
851 566 (2004).
852
- 853 6. Assareh N, Bagley EE, Carrive P, McNally GP. Brief optogenetic inhibition of rat lateral or
854 ventrolateral periaqueductal gray augments the acquisition of Pavlovian fear conditioning.
855 *Behav Neurosci* **131**, 454-459 (2017).
856
- 857 7. Assareh N, Sarrami M, Carrive P, McNally GP. The organization of defensive behavior
858 elicited by optogenetic excitation of rat lateral or ventrolateral periaqueductal gray. *Behav*
859 *Neurosci* **130**, 406-414 (2016).
860
- 861 8. Falkner AL, *et al.* Hierarchical Representations of Aggression in a Hypothalamic-Midbrain
862 Circuit. *Neuron* **106**, 637-648 e636 (2020).
863
- 864 9. Xiao Z, Ou S, He WJ, Zhao YD, Liu XH, Ruan HZ. Role of midbrain periaqueductal gray
865 P2X3 receptors in electroacupuncture-mediated endogenous pain modulatory systems.
866 *Brain Res* **1330**, 31-44 (2010).
867
- 868 10. Dampney RA, Furlong TM, Horiuchi J, Iigaya K. Role of dorsolateral periaqueductal grey
869 in the coordinated regulation of cardiovascular and respiratory function. *Auton Neurosci*
870 **175**, 17-25 (2013).
871
- 872 11. Miranda-Paiva CM, Canteras NS, Sukikara MH, Nasello AG, Mackowiak II, Felicio LF.
873 Periaqueductal gray cholecystokinin infusions block morphine-induced disruption of
874 maternal behavior. *Peptides* **28**, 657-662 (2007).
875
- 876 12. Mota-Ortiz SR, *et al.* The periaqueductal gray as a critical site to mediate reward seeking
877 during predatory hunting. *Behav Brain Res* **226**, 32-40 (2012).
878

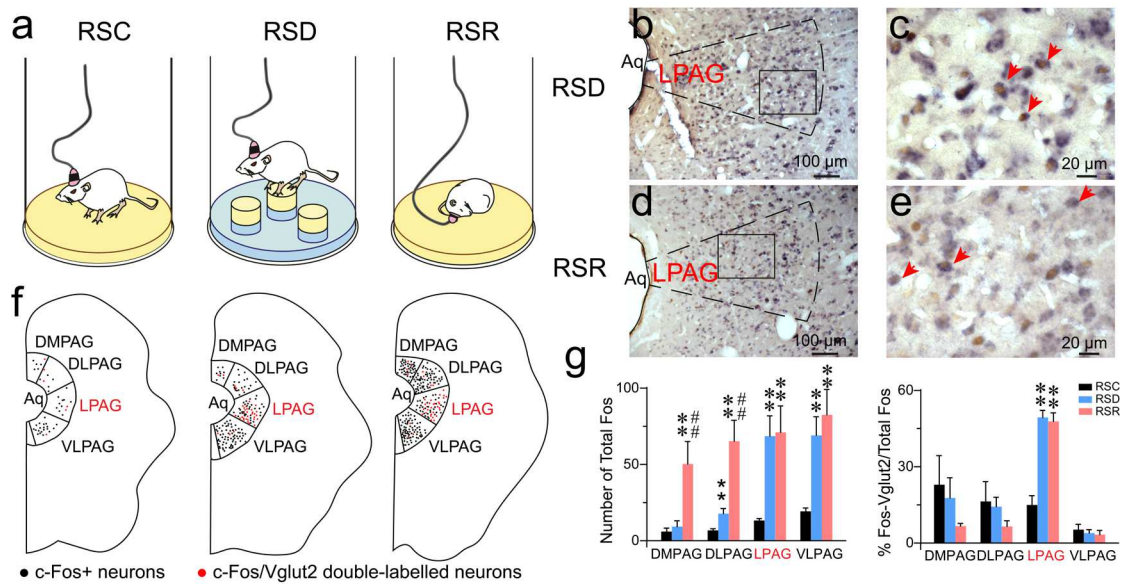
- 879 13. Faull OK, Pattinson KT. The cortical connectivity of the periaqueductal gray and the
880 conditioned response to the threat of breathlessness. *Elife* **6**, (2017).
881
- 882 14. Yu H, *et al.* Periaqueductal gray neurons encode the sequential motor program in hunting
883 behavior of mice. *Nat Commun* **12**, 6523 (2021).
884
- 885 15. Chiang MC, Nguyen EK, Canto-Bustos M, Papale AE, Oswald AM, Ross SE. Divergent
886 Neural Pathways Emanating from the Lateral Parabrachial Nucleus Mediate Distinct
887 Components of the Pain Response. *Neuron* **106**, 927-939 e925 (2020).
888
- 889 16. Wang H, *et al.* Direct auditory cortical input to the lateral periaqueductal gray controls
890 sound-driven defensive behavior. *PLoS Biol* **17**, e3000417 (2019).
891
- 892 17. Fujisaki M, Hashimoto K, Iyo M, Chiba T. Role of the amygdalo-hippocampal transition
893 area in the fear expression: evaluation by behavior and immediate early gene expression.
894 *Neuroscience* **124**, 247-260 (2004).
895
- 896 18. Sapin E, *et al.* Localization of the brainstem GABAergic neurons controlling paradoxical
897 (REM) sleep. *PLoS One* **4**, e4272 (2009).
898
- 899 19. Billwiller F, Renouard L, Clement O, Fort P, Luppi PH. Differential origin of the activation
900 of dorsal and ventral dentate gyrus granule cells during paradoxical (REM) sleep in the rat.
901 *Brain Struct Funct* **222**, 1495-1507 (2017).
902
- 903 20. Luo YJ, *et al.* Nucleus accumbens controls wakefulness by a subpopulation of neurons
904 expressing dopamine D1 receptors. *Nat Commun* **9**, 1576 (2018).
905
- 906 21. Zhang Z, *et al.* Superior Colliculus GABAergic Neurons Are Essential for Acute Dark
907 Induction of Wakefulness in Mice. *Curr Biol* **29**, 637-644 e633 (2019).
908
- 909 22. Liu Y, *et al.* A circuit from dorsal hippocampal CA3 to paraventricular nucleus mediates chronic
910 social defeat stress-induced deficits in preference for social novelty. *Sci Adv* **8**, eabe8828
911 (2022).
912
- 913 23. Wang S, Veinot J, Goyal A, Khatibi A, Lazar SW, Hashmi JA. Distinct networks of
914 periaqueductal gray columns in pain and threat processing. *Neuroimage* **250**, 118936
915 (2022).
916
- 917 24. Arico C, Bagley EE, Carrive P, Assareh N, McNally GP. Effects of chemogenetic excitation
918 or inhibition of the ventrolateral periaqueductal gray on the acquisition and extinction of
919 Pavlovian fear conditioning. *Neurobiol Learn Mem* **144**, 186-197 (2017).
920
- 921 25. Faull OK, Jenkinson M, Ezra M, Pattinson K. Conditioned respiratory threat in the
922 subdivisions of the human periaqueductal gray. *Elife* **5**, (2016).

- 923
- 924 26. Vazquez-Leon P, Miranda-Paez A, Chavez-Reyes J, Allende G, Barragan-Iglesias P,
925 Marichal-Cancino BA. The Periaqueductal Gray and Its Extended Participation in Drug
926 Addiction Phenomena. *Neurosci Bull* **37**, 1493-1509 (2021).
927
- 928 27. Jouvet M. Neurophysiology of the states of sleep. *Physiol Rev* **47**, 117-177 (1967).
929
- 930 28. Chase MH. Synaptic mechanisms and circuitry involved in motoneuron control during
931 sleep. *Int Rev Neurobiol* **24**, 213-258 (1983).
932
- 933 29. Wang YQ, Liu WY, Li L, Qu WM, Huang ZL. Neural circuitry underlying REM sleep: A review
934 of the literature and current concepts. *Prog Neurobiol* **204**, 102106 (2021).
935
- 936 30. Pham J, Cabrera SM, Sanchis-Segura C, Wood MA. Automated scoring of fear-related
937 behavior using EthoVision software. *J Neurosci Methods* **178**, 323-326 (2009).
938
- 939 31. Watson TC, Cerminara NL, Lumb BM, Apps R. Neural Correlates of Fear in the
940 Periaqueductal Gray. *J Neurosci* **36**, 12707-12719 (2016).
941
- 942 32. Steenland HW, Zhuo M. Neck electromyography is an effective measure of fear behavior.
943 *J Neurosci Methods* **177**, 355-360 (2009).
944
- 945 33. Kim JH, Gangadharan G, Byun J, Choi EJ, Lee CJ, Shin HS. Yin-and-yang bifurcation of
946 opioidergic circuits for descending analgesia at the midbrain of the mouse. *Proc Natl Acad
947 Sci U S A* **115**, 11078-11083 (2018).
948
- 949 34. Okai H, Okazaki R, Kawamura M, Yoshimura M. Excitatory effect of Neurotrophin((R)) on
950 noradrenergic neurons in rat locus coeruleus. *Life Sci* **136**, 79-86 (2015).
951
- 952 35. Dahlstroem A, Fuxe K. Evidence for the Existence of Monoamine-Containing Neurons in
953 the Central Nervous System. I. Demonstration of Monoamines in the Cell Bodies of Brain
954 Stem Neurons. *Acta Physiol Scand Suppl*, SUPPL 232:231-255 (1964).
955
- 956 36. Carter ME, *et al.* Tuning arousal with optogenetic modulation of locus coeruleus neurons.
957 *Nat Neurosci* **13**, 1526-1533 (2010).
958
- 959 37. Berridge CW. Noradrenergic modulation of arousal. *Brain Res Rev* **58**, 1-17 (2008).
960
- 961 38. Takahashi K, Kayama Y, Lin JS, Sakai K. Locus coeruleus neuronal activity during the sleep-
962 waking cycle in mice. *Neuroscience* **169**, 1115-1126 (2010).
963
- 964 39. Devilbiss DM, Page ME, Waterhouse BD. Locus ceruleus regulates sensory encoding by
965 neurons and networks in waking animals. *J Neurosci* **26**, 9860-9872 (2006).
966

- 967 40. Grella SL, *et al.* Locus Coeruleus Phasic, But Not Tonic, Activation Initiates Global
968 Remapping in a Familiar Environment. *J Neurosci* **39**, 445-455 (2019).
969
- 970 41. Aston-Jones G, Bloom FE. Activity of norepinephrine-containing locus coeruleus neurons
971 in behaving rats anticipates fluctuations in the sleep-waking cycle. *J Neurosci* **1**, 876-886
972 (1981).
973
- 974 42. Aston-Jones G, *et al.* Afferent regulation of locus coeruleus neurons: anatomy, physiology
975 and pharmacology. *Prog Brain Res* **88**, 47-75 (1991).
976
- 977 43. Kaitin KI, Bliwise DL, Gleason C, Nino-Murcia G, Dement WC, Libet B. Sleep disturbance
978 produced by electrical stimulation of the locus coeruleus in a human subject. *Biol*
979 *Psychiatry* **21**, 710-716 (1986).
980
- 981 44. Soya S, *et al.* Orexin modulates behavioral fear expression through the locus coeruleus.
982 *Nat Commun* **8**, 1606 (2017).
983
- 984 45. Sakai K, Sastre JP, Salvat D, Touret M, Tohyama M, Jouvet M. Tegmentoreticular
985 projections with special reference to the muscular atonia during paradoxical sleep in the
986 cat: an HRP study. *Brain Res* **176**, 233-254 (1979).
987
- 988 46. Fort P, Luppi PH, Wenthold R, Jouvet M. [Glycine immunoreactive neurons in the medulla
989 oblongata in cats]. *C R Acad Sci III* **311**, 205-212 (1990).
990
- 991 47. Sakai K, Crochet S, Onoe H. Pontine structures and mechanisms involved in the generation
992 of paradoxical (REM) sleep. *Arch Ital Biol* **139**, 93-107 (2001).
993
- 994 48. Valencia Garcia S, Libourel PA, Lazarus M, Grassi D, Luppi PH, Fort P. Genetic inactivation
995 of glutamate neurons in the rat sublateralodorsal tegmental nucleus recapitulates REM
996 sleep behaviour disorder. *Brain* **140**, 414-428 (2017).
997
- 998 49. Weber F, Chung S, Beier KT, Xu M, Luo L, Dan Y. Control of REM sleep by ventral medulla
999 GABAergic neurons. *Nature* **526**, 435-438 (2015).
1000
- 1001 50. Tovote P, *et al.* Midbrain circuits for defensive behaviour. *Nature* **534**, 206-212 (2016).
1002
- 1003 51. Luppi PH, *et al.* Paradoxical (REM) sleep genesis: the switch from an aminergic-cholinergic
1004 to a GABAergic-glutamatergic hypothesis. *J Physiol Paris* **100**, 271-283 (2006).
1005
- 1006 52. Allen WE, *et al.* Thirst-associated preoptic neurons encode an aversive motivational drive.
1007 *Science* **357**, 1149-1155 (2017).
1008
- 1009 53. DeNardo LA, *et al.* Temporal evolution of cortical ensembles promoting remote memory
1010 retrieval. *Nat Neurosci* **22**, 460-469 (2019).

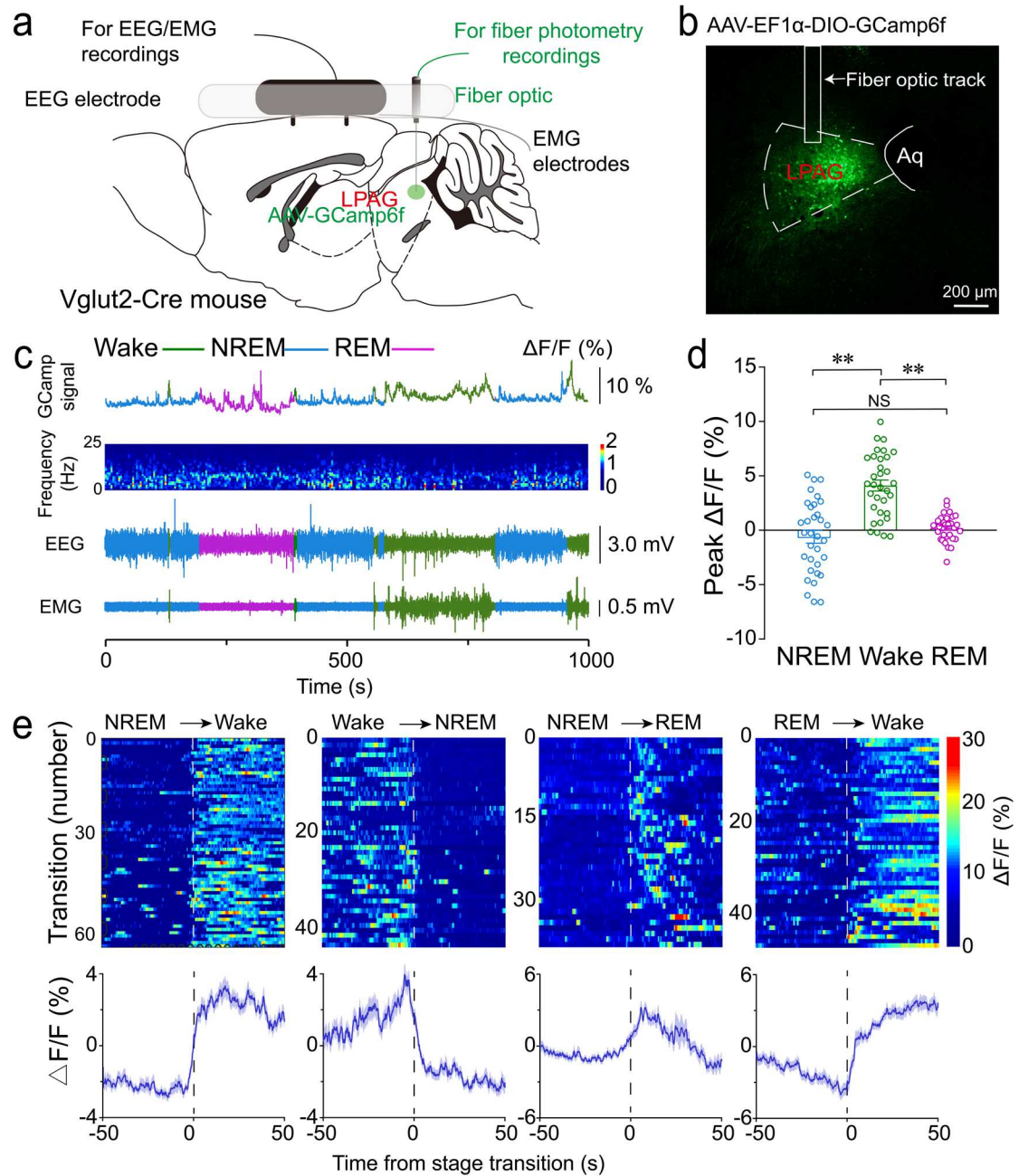
- 1011
- 1012 54. Li L, Zhang MQ, Sun X, Liu WY, Huang ZL, Wang YQ. Role of Dorsomedial Hypothalamus
1013 GABAergic Neurons in Sleep-Wake States in Response to Changes in Ambient
1014 Temperature in Mice. *Int J Mol Sci* **23**, (2022).
- 1015
- 1016 55. Wang YQ, *et al.* Adenosine A2A receptors in the olfactory bulb suppress rapid eye
1017 movement sleep in rodents. *Brain Struct Funct* **222**, 1351-1366 (2017).
- 1018
- 1019 56. Qu WM, Xu XH, Yan MM, Wang YQ, Urade Y, Huang ZL. Essential role of dopamine D2
1020 receptor in the maintenance of wakefulness, but not in homeostatic regulation of sleep,
1021 in mice. *J Neurosci* **30**, 4382-4389 (2010).
- 1022
- 1023 57. Shen Y, *et al.* Propagated alpha-synucleinopathy recapitulates REM sleep behaviour
1024 disorder followed by parkinsonian phenotypes in mice. *Brain* **143**, 3374-3392 (2020).
- 1025
- 1026 58. Valencia Garcia S, *et al.* Ventromedial medulla inhibitory neuron inactivation induces REM
1027 sleep without atonia and REM sleep behavior disorder. *Nat Commun* **9**, 504 (2018).
- 1028
- 1029 59. Arthaud S, *et al.* Paradoxical (REM) sleep deprivation in mice using the small-platforms-
1030 over-water method: polysomnographic analyses and melanin-concentrating hormone
1031 and hypocretin/orexin neuronal activation before, during and after deprivation. *J Sleep*
1032 *Res* **24**, 309-319 (2015).
- 1033
- 1034 60. Lee HS, *et al.* Targeted recombination in active populations as a new mouse genetic model
1035 to study sleep-active neuronal populations: Demonstration that Lhx6+ neurons in the
1036 ventral zona incerta are activated during paradoxical sleep hypersomnia. *J Sleep Res* **29**,
1037 e12976 (2020).
- 1038
- 1039 61. Libourel PA, Corneillie A, Luppi PH, Chouvet G, Gervasoni D. Unsupervised online
1040 classifier in sleep scoring for sleep deprivation studies. *Sleep* **38**, 815-828 (2015).
- 1041
- 1042 62. Arthaud S, Libourel PA, Luppi PH, Peyron C. Insights into paradoxical (REM) sleep
1043 homeostatic regulation in mice using an innovative automated sleep deprivation method.
1044 *Sleep* **43**, (2020).
- 1045
- 1046 63. Verret L, *et al.* A role of melanin-concentrating hormone producing neurons in the central
1047 regulation of paradoxical sleep. *BMC Neurosci* **4**, 19 (2003).
- 1048
- 1049 64. Dong H, Wang J, Yang YF, Shen Y, Qu WM, Huang ZL. Dorsal Striatum Dopamine Levels
1050 Fluctuate Across the Sleep-Wake Cycle and Respond to Salient Stimuli in Mice. *Front*
1051 *Neurosci* **13**, 242 (2019).
- 1052
- 1053 65. Yang YF, *et al.* Mesencephalic dopamine neurons are essential for modafinil-induced
1054 arousal. *Br J Pharmacol* **178**, 4808-4825 (2021).

- 1055
1056 66. Seibenhener ML, Wooten MC. Use of the Open Field Maze to measure locomotor and
1057 anxiety-like behavior in mice. *J Vis Exp*, e52434 (2015).
1058
1059 67. Xu W, *et al.* Sevoflurane depresses neurons in the medial parabrachial nucleus by
1060 potentiating postsynaptic GABAA receptors and background potassium channels.
1061 *Neuropharmacology* **181**, 108249 (2020).
1062
1063 68. Liu G, Wang Y, Zheng W, Cheng H, Zhou R. P11 Loss-of-Function is Associated with
1064 Decreased Cell Proliferation and Neurobehavioral Disorders in Mice. *Int J Biol Sci* **15**,
1065 1383-1395 (2019).
1066
1067 69. Li R, *et al.* Activation of adenosine A2A receptors in the olfactory tubercle promotes sleep
1068 in rodents. *Neuropharmacology* **168**, 107923 (2020).
1069



1070
 1071
 1072
 1073
 1074
 1075
 1076
 1077
 1078
 1079
 1080
 1081
 1082
 1083
 1084
 1085
 1086
 1087

Fig. 1 Lateral periaqueductal gray (LPAG) neurons expressing c-Fos during rapid eye movement (REM) sleep deprivation (RSD) and REM sleep rebound (RSR) are glutamatergic. **a** Scheme for the rats submitted to 72-h protocol of control (RSC), RSD, and RSR using the flowerpot method. **b–e** Photomicrographs showing c-Fos (brown nuclear stained) and Vglut2 (blue diffuse cytoplasmic stained) double-stained neurons in the LPAG of the RSD (**b, c**) and RSR (**d, e**) rats. **c** and **e** show the area inside the rectangle in **b** and **d** at a higher magnification. The red arrowheads indicate the double-labeled neurons in the LPAG. Scale bars: 100 μ m in **b** and **d** and 20 μ m in **c** and **e**. **f** Schematic distribution of single c-Fos+ (black dots) and double-labeled (c-Fos+/Vglut2+, red dots) neurons on a coronal section in representative animals under RSC, RSD, and RSR conditions. **g** Histogram showing the numbers of single c-Fos+ and the percentage of double-labeled (c-Fos+/Vglut2+) neurons within the LPAG and neighboring areas under each experimental condition. Values are presented as means \pm standard error of mean (SEM) ($n = 4$). ** $p < 0.01$ compared to RSC animals, ### $p < 0.01$ compared to RSD animals, using one-way ANOVA followed by Tukey's post hoc test.



1088

1089 **Fig. 2 Population activity of LPAG^{Vglut2} neurons across sleep-wake states. a**

1090 Schematic of *in vivo* fiber photometry recordings. **b** Unilateral viral targeting of AAV-

1091 EF1 α -DIO-GCaMP6f into the LPAG of Vglut2-Cre mouse and the tip of the fiber optic

1092 located above the LPAG. Scale bar: 200 μ m. **c** Representative fluorescent traces,

1093 relative electroencephalography (EEG) power, and EEG/electromyography (EMG)

1094 traces across spontaneous sleep-wake states. **d** $\Delta F/F$ peaks during non-REM (NREM)

1095 sleep, wakefulness, and REM sleep. The fluorescent peak value was normalized by

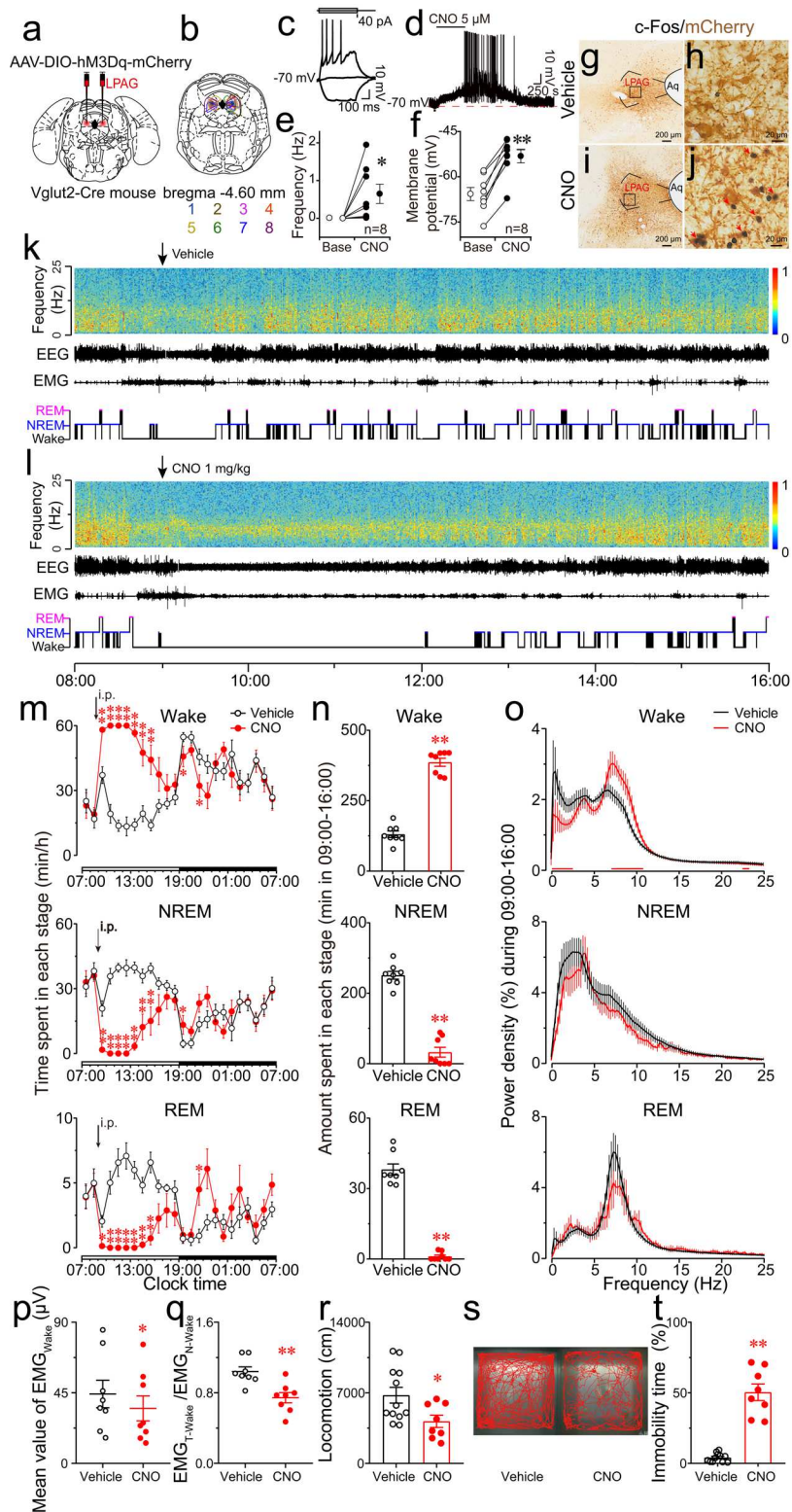
1096 mean $\Delta F/F$ peaks in NREM sleep ($n = 3$ mice, 11 sessions per mouse, $** p < 0.01$, one-

1097 way ANOVA followed by Tukey's post hoc test). **e** Fluorescent signals aligned with

1098 sleep–wake transitions. Upper panel: Individual transitions with color-coded
1099 fluorescent intensities. Lower panel: Average calcium transients from the transitions
1100 expressed as mean \pm SEM.

1101

1102

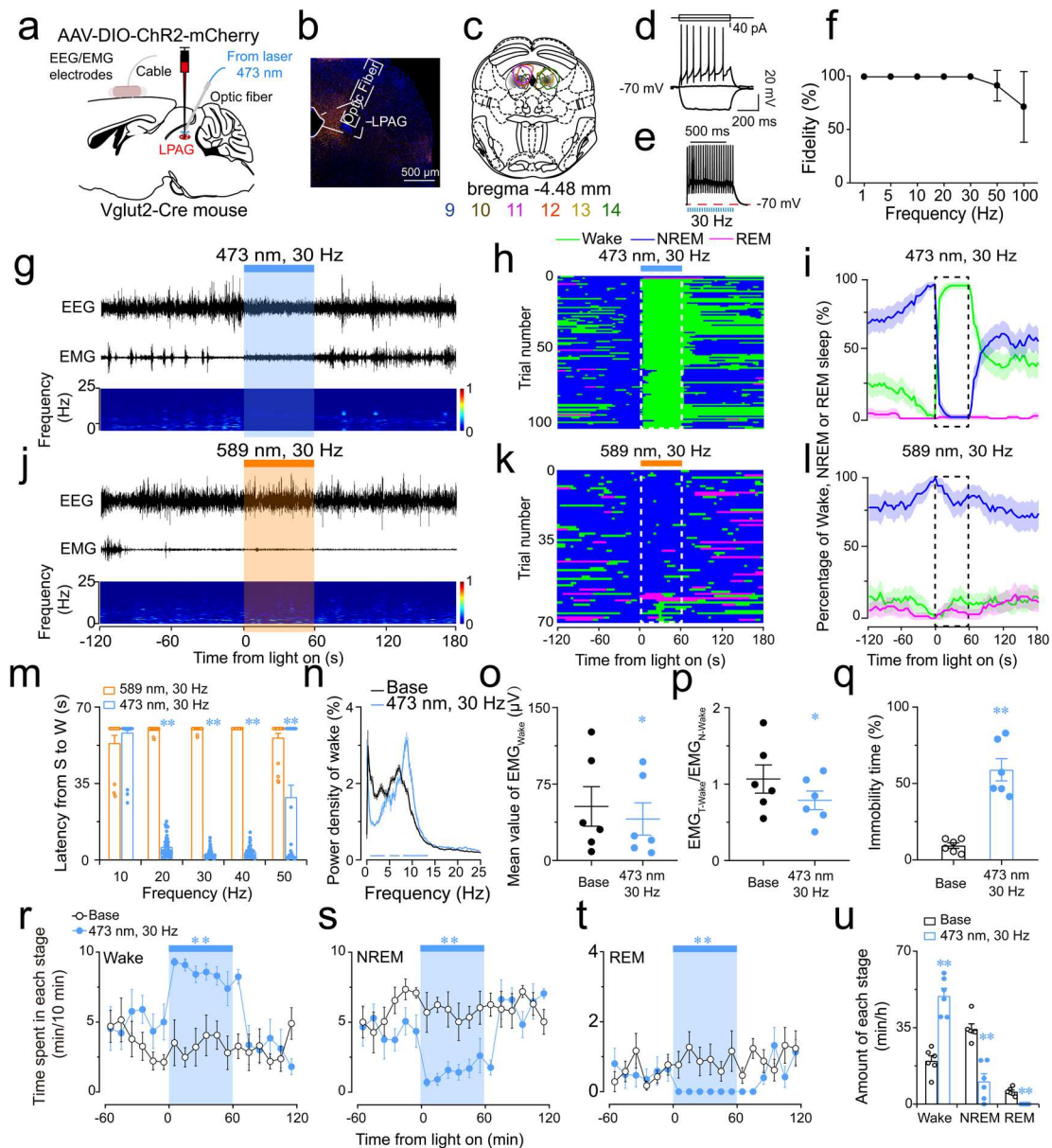


1103

1104 **Fig. 3 Chemogenetic activation of LPAg^{Vglut2} neurons promotes wakefulness and**
 1105 **immobility.** **a** Vglut2-Cre mice were infused with AAV expressing hM3Dq in a Cre-
 1106 dependent manner under the control of the Vglut2 promoter. **b** Drawings of

1107 superimposed AAV-injected areas in the LPAG of Vglut2-Cre mice ($n = 8$, indicated
1108 with different colors). **c** Membrane potential changes induced by current injection in a
1109 non-spontaneous firing neuron. Resting membrane potential: -70 mV. **d** Typical
1110 example of membrane potential recorded from an hM3Dq-expressing Vglut2 neuron
1111 during the application of clozapine-N-oxide (CNO) to brain slices. Bath application of
1112 CNO ($5 \mu\text{M}$) produced depolarization and firing. **e, f** CNO induced a significant
1113 increase in firing frequency and depolarization in eight Vglut2 neurons. Individual and
1114 average values of the firing frequency (**e**) and membrane potential (**f**) are shown on the
1115 scatter plot. **g-j** Typical samples of two LPAG-hM3Dq mice injected with either vehicle
1116 (**g, h**) or CNO (**i, j**). The full line rectangle areas in **g** and **i** were magnified (**h, j**) to
1117 demonstrate the co-expression of hM3Dq fusion protein mCherry and c-Fos, which is
1118 indicated by red arrows. **k, l** Typical examples of one LPAG-hM3Dq mouse each
1119 injected (i.p.) with vehicle (**k**) and CNO at 1 mg/kg (**l**). **m** Time course of wakefulness,
1120 NREM sleep and REM sleep in Vglut2-Cre mice expressing hM3Dq after
1121 administration of vehicle or CNO. **n** The total time spent in wakefulness, NREM sleep,
1122 and REM sleep in Vglut2-Cre mice expressing hM3Dq for 7 h after administration of
1123 vehicle or CNO. **o** EEG power density for 7 h after administration of vehicle or CNO.
1124 The power of each 0.25-Hz bin was averaged and normalized by calculating the
1125 percentage of each bin from the total power (0–25 Hz). The horizontal bars indicate
1126 statistical differences ($p < 0.05$). **p** Quantification and comparison of the EMG_{Wake} (the
1127 EMG amplitude during wakefulness) between vehicle and CNO groups. **q** The ratio of
1128 $\text{EMG}_{\text{T-Wake}}$ (the EMG amplitude during wakefulness after treatment with vehicle or
1129 CNO) and $\text{EMG}_{\text{N-Wake}}$ (the EMG amplitude during the normal wakefulness stage)
1130 between the vehicle and CNO groups. **r** The locomotor activity in Vglut2-Cre mice
1131 expressing hM3Dq for 15 min after administration of vehicle or CNO. **s** A
1132 representative trajectory plot of a Vglut2-Cre mouse after administration of vehicle or
1133 CNO. **t** Mean immobility time in Vglut2-Cre mice expressing hM3Dq for 15 min after
1134 administration of vehicle or CNO. Data are presented as mean \pm SEM ($n = 8\text{--}12$). Each
1135 dot indicates data from a single mouse. * $p < 0.05$, ** $p < 0.01$, compared to the vehicle

1136 group, using repeated measures ANOVA followed by a paired *t*-test (**m**), a paired *t*-test
1137 (**e, f, n, o-q**), and one-way ANOVA followed by Tukey's post hoc test (**r, t**).
1138
1139



1140

1141

Fig. 4 Optogenetic activation of LPAG^{Vglut2} neurons induces wakefulness and

1142

immobility. a Vglut2-Cre mice injected with AAV-DIO-ChR2-mCherry into the LPAG.

1143

b Representative images of mCherry immunofluorescence in the LPAG. Scale bar: 500

1144

μm . **c** Drawings of superimposed AAV-injected areas in the LPAG of Vglut2-Cre mice

1145

($n = 6$, indicated with different colors). **d** The electrophysiological properties of the

1146

recorded Vglut2 neuron. **e** The responses of ChR2-expressing Vglut2 neuron in the

1147

LPAG to 5-ms blue light (473 nm) photostimulation at 30 Hz. **f** Fidelity responses of

1148

the recorded ChR2-expressing Vglut2 neurons in the LPAG to blue light pulses at

1149

frequencies up to 100 Hz. **g, j** Representative EEG/EMG traces and heat map of EEG

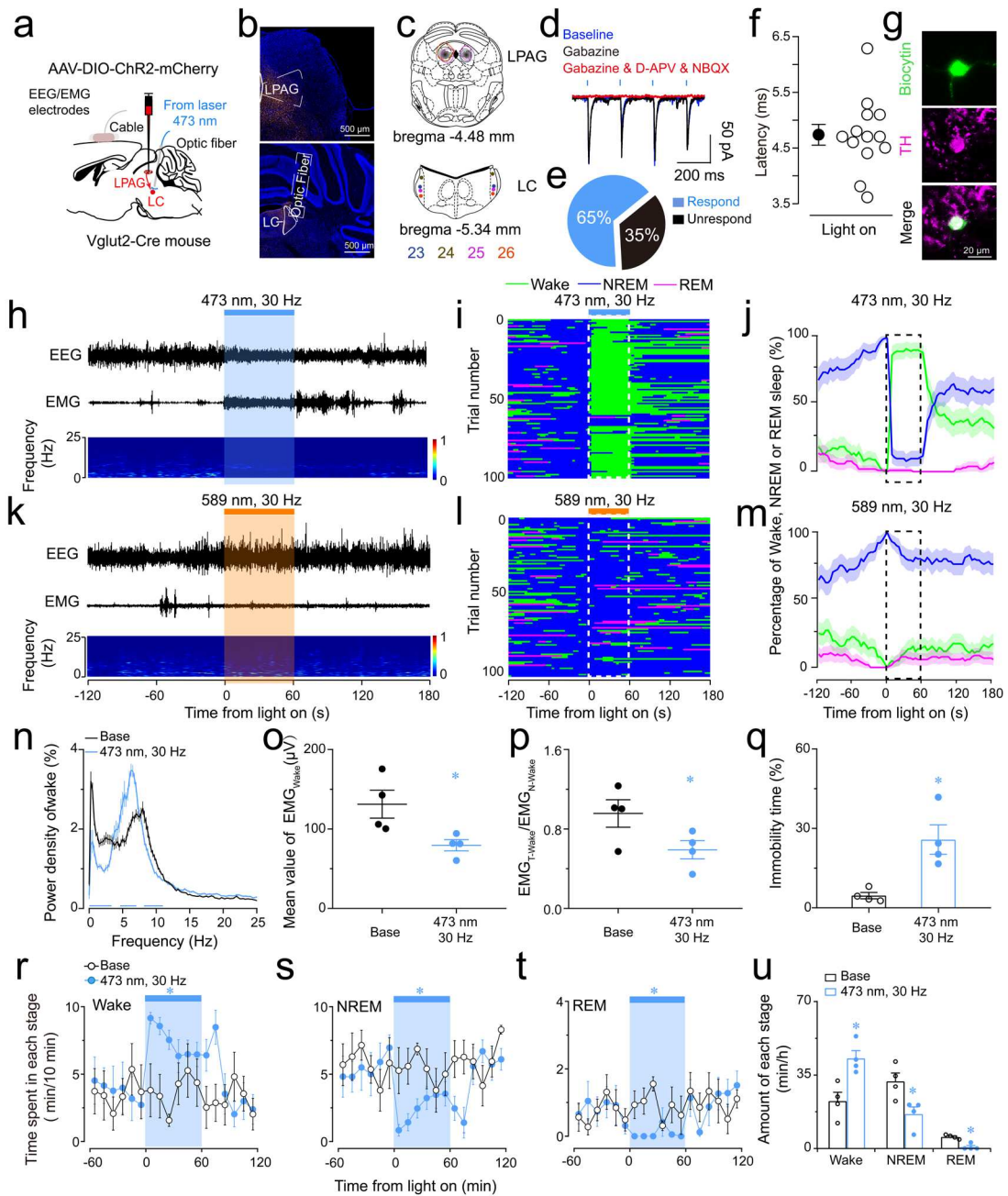
1150

power spectra showing acute photostimulation (30 Hz/5 ms) of blue (**g**) and yellow (**j**)

1151 light applied during NREM sleep in a ChR2-mcherry mouse. **h, i, k, l** Sleep stages after
1152 blue (**h, i**) and yellow (**k, l**) light stimulation in ChR2-mCherry mice. **m** Latencies of
1153 transitions from NREM sleep (S) to wakefulness (W) after photostimulation at different
1154 frequencies. **n** EEG power density before and after the photostimulation in ChR2-
1155 mCherry mice. The power of each 0.25-Hz bin was averaged and normalized by
1156 calculating the percentage of each bin from the total power (0–25 Hz). The horizontal
1157 bars indicate statistical differences ($p < 0.05$). **o** Quantification and comparison of the
1158 EMG_{Wake} (the integral muscle tone intensity during wakefulness) before and after the
1159 photostimulation in ChR2-mCherry mice. **p** The ratio of EMG_{T-Wake} (the EMG
1160 amplitude during wakefulness before and after treatment with blue light) and EMG<sub>N-
1161 wake</sub> (the EMG amplitude during normal wakefulness stage) before and after the
1162 photostimulation in ChR2-mCherry mice. **q** Mean immobility time during base and
1163 blue light stimulation in ChR2-mcherry mice. **r-t** Time course of wakefulness (**r**),
1164 NREM sleep (**s**), and REM sleep (**t**) during a semi-chronic optogenetic experiment (30
1165 Hz/5 ms, 40 s on/20 s off) before and after the photostimulation in ChR2-mCherry mice.
1166 **u** Total amounts of each stage before and after the photostimulation in ChR2-mCherry
1167 mice. Data are presented as mean \pm SEM ($n = 6$). Each dot indicates data from a single
1168 mouse. * $p < 0.05$, ** $p < 0.01$, compared to yellow light (**m**) and the base group (**n-u**),
1169 using repeated measures ANOVA followed by a paired t -test (**r-t**) or paired t -test (**m-q**,
1170 **u**).

1171

1172



1173

1174 **Fig. 5 Optogenetic stimulation of the LPAG^{Vglut2}-LC pathway induces wakefulness**

1175 **and immobility.** **a** Schematic drawing shows ChR2-expressing LPAG and the targeted

1176 downstream nuclei, the locus coeruleus (LC). **b** Representative images of the mCherry

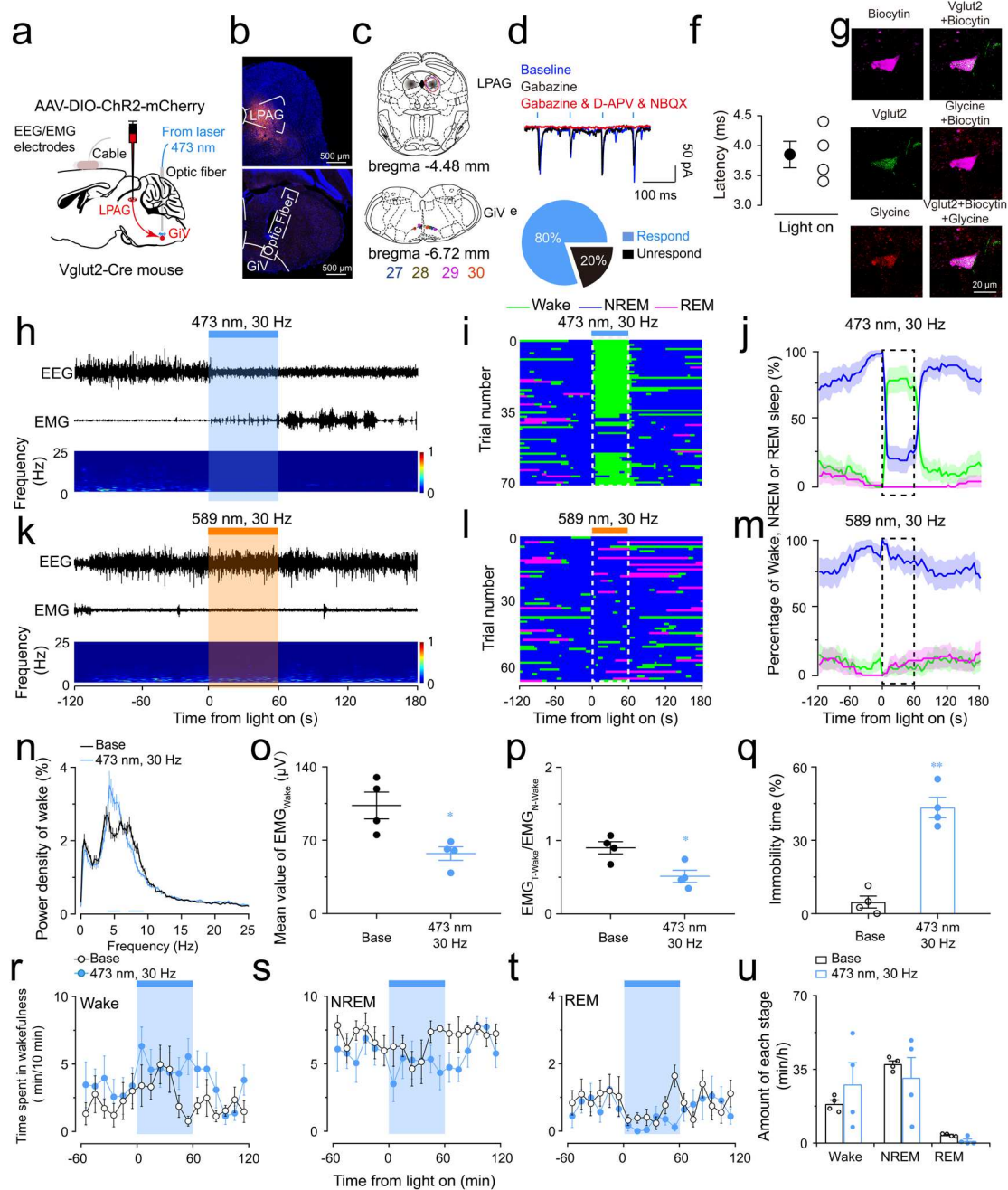
1177 immunofluorescence in LPAG and the terminals in the LC from the LPAG^{Vglut2} neurons.

1178 Scale bar: 500 μ m. **c** Diagrams of superimposed AAV-injected areas in LPAG and the

1179 terminals in the LC of Vglut2-Cre mice ($n = 4$, indicated with different colors). **d**

1180 Typical traces representing the inward current elicited by photostimulation of ChR2-

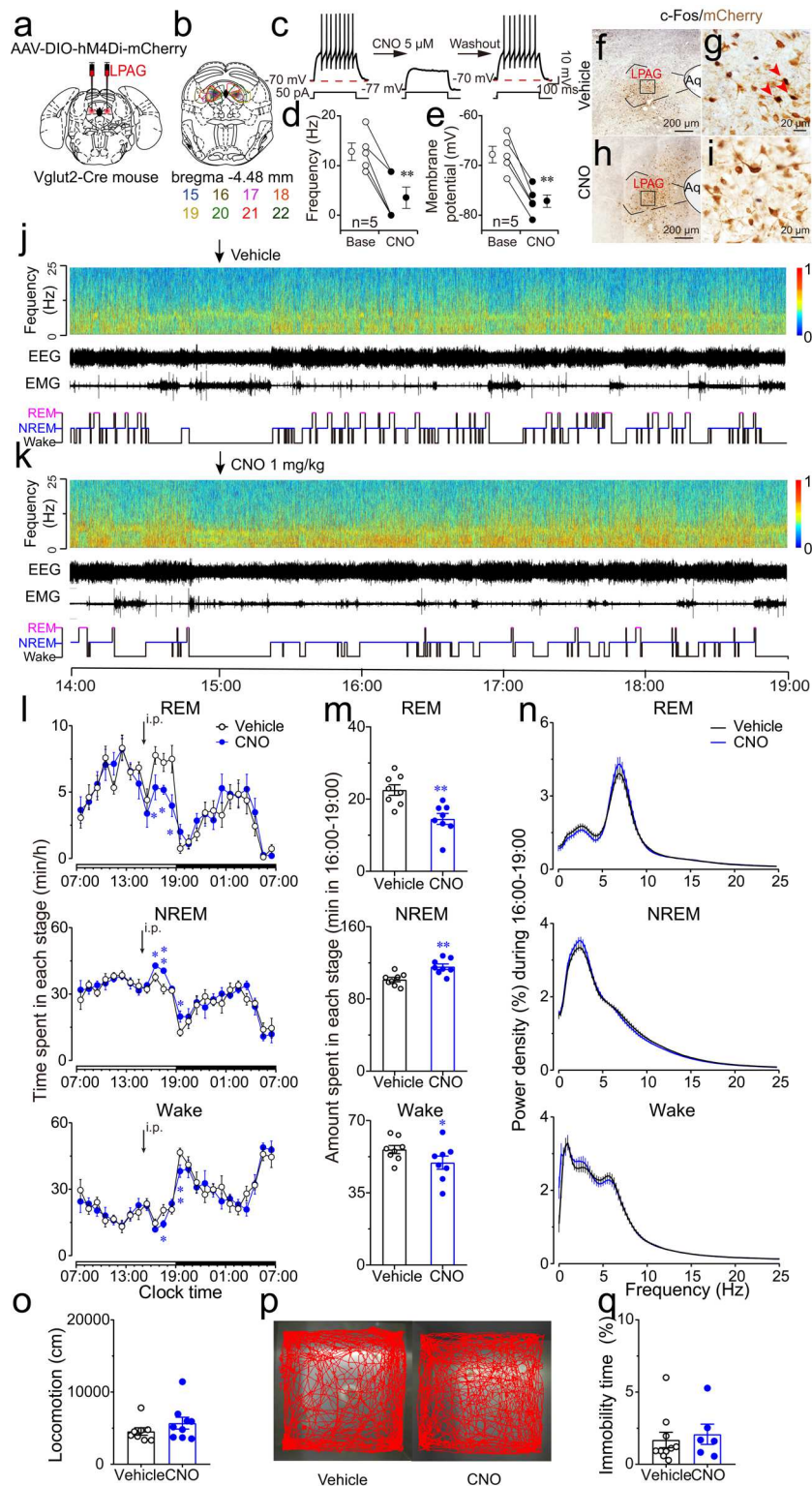
1181 expressing LPAG axons at the LC under different conditions. **e** The proportion of
1182 recorded LC neurons that did and did not respond to the photostimulation of ChR2-
1183 expressing LPAG terminals. **f** The latency between the delivery of photostimulation and
1184 the firing event of the responding LC neurons are summarized. **g** Typical example of a
1185 connected biocytin-labeled neuron that was tyrosine hydroxylase (TH)-positive. Scale
1186 bar: 20 μ m. **h, k** Representative EEG/EMG traces and heat map of EEG power spectra
1187 showing acute photostimulation (30 Hz/5 ms) of the LPAG^{Vglut2}-LC pathway with blue
1188 (**h**) and yellow (**k**) light applied during NREM sleep in a ChR2-mcherry mouse. **i, j, l,**
1189 **m** Sleep stages after blue (**i, j**) and yellow light (**l, m**) stimulation of the LPAG^{Vglut2}-LC
1190 pathway in ChR2-mCherry mice. **n** EEG power density before and after
1191 photostimulation of the LPAG^{Vglut2}-LC pathway in ChR2-mCherry mice. The power of
1192 each 0.25-Hz bin was averaged and normalized by calculating the percentage of each
1193 bin from the total power (0–25 Hz). The horizontal bars indicate statistical differences
1194 ($p < 0.05$). **o** Quantification and comparison of the EMG_{Wake} (the integral muscle tone
1195 intensity during wakefulness) before and after photostimulation of the LPAG^{Vglut2}-LC
1196 pathway in ChR2-mCherry mice. **p** The ratio of EMG_{T-Wake} (the EMG amplitude during
1197 wakefulness before and after treatment with blue light) and EMG_{N-Wake} (the EMG
1198 amplitude during normal wakefulness stage) before and after photostimulation of the
1199 LPAG^{Vglut2}-LC pathway in ChR2-mCherry mice. **q** Mean immobility time during base
1200 and blue light stimulation of the LPAG^{Vglut2}-LC pathway in ChR2-mcherry mice. **r, s, t**
1201 Time course of wakefulness (**r**), NREM) sleep (**s**) and REM sleep (**t**) during semi-
1202 chronic optogenetic experiment (30 Hz/5 ms, 40 s on/20 s off) before and after
1203 photostimulation of the LPAG^{Vglut2}-LC pathway in ChR2-mCherry mice. **u**, Total
1204 amounts of each sleep stage before and after photostimulation of the LPAG^{Vglut2}-LC
1205 pathway in ChR2-mCherry mice. Data are presented as the mean \pm SEM. Each dot
1206 indicates data from a single mouse ($n = 4$). * $p < 0.05$, ** $p < 0.01$, compared to the
1207 base group (**n-u**), using repeated measures ANOVA followed by a paired t -test (**r-t**) or
1208 paired t -test (**n-q, u**).
1209



1210

1211 **Fig. 6 Optogenetic stimulation of the LPAG^{Vglut2}-GiV pathway induces**
 1212 **wakefulness and immobility.** **a** Schematic drawing shows ChR2-expressing LPAG
 1213 and the targeted downstream nuclei, the ventral gigantocellular reticular nucleus (GiV).
 1214 **b** Representative images of the mCherry immunofluorescence in LPAG and the
 1215 terminals in the GiV from the LPAG^{Vglut2} neurons. Scale bar: 500 μm. **c** Diagrams of
 1216 superimposed AAV-injected areas in LPAG and the terminals in the GiV of Vglut2-Cre
 1217 mice (*n* = 4, indicated with different colors). **d** Typical traces representing the inward

1218 current elicited by photostimulation of Chr2-expressing LPAG axons at the GiV under
1219 different conditions. **e**, The proportion of recorded GiV neurons that did and did not
1220 respond to photostimulation of Chr2-expressing LPAG terminals. **f** The latency
1221 between the delivery of photostimulation and the firing event of the responding GiV
1222 neurons are summarized. **g** Typical example of a connected biocytin-labeled neuron
1223 that was Vglut2- and glycine-positive. Scale bar: 20 μ m. **h, k** Representative
1224 EEG/EMG traces and heat map of EEG power spectra showing that acute
1225 photostimulation (30 Hz/5 ms) of the LPAG^{Vglut2}-GiV pathway with blue (**h**) and yellow
1226 (**k**) light applied during non-rapid eye movement (NREM) sleep in a Chr2-mcherry
1227 mouse. **i, j, l, m** Sleep stages after blue (**i, j**) and yellow light (**l, m**) stimulation of the
1228 LPAG^{Vglut2}-GiV pathway in Chr2-mCherry mice. **n** EEG power density before and
1229 after photostimulation of the LPAG^{Vglut2}-GiV pathway in Chr2-mCherry mice. The
1230 power of each 0.25-Hz bin was averaged and normalized by calculating the percentage
1231 of each bin from the total power (0–25 Hz). The horizontal bars indicate statistical
1232 differences ($p < 0.05$). **o** Quantification and comparison of the EMG_{Wake} (the EMG
1233 amplitude during wakefulness) before and after photostimulation of the LPAG^{Vglut2}-
1234 GiV pathway in Chr2-mCherry mice. **p** The ratio of EMG_{T-Wake} (the EMG amplitude
1235 during wakefulness before and after treatment with blue light) and EMG_{N-Wake} (the
1236 EMG amplitude during the normal wakefulness stage) before and after
1237 photostimulation of the LPAG^{Vglut2}-GiV pathway in Chr2-mCherry mice. **q** Mean
1238 immobility time during base and blue light stimulation of the LPAG^{Vglut2}-GiV pathway
1239 in Chr2-mCherry mice. **r-t** Time course of wakefulness (**r**), NREM sleep (**s**), and REM
1240 sleep (**t**) during semi-chronic optogenetic experiment (30 Hz/5 ms, 40 s on/20 s off)
1241 before and after photostimulation of the LPAG^{Vglut2}-GiV pathway in Chr2-mCherry
1242 mice. **u** Total amounts of each sleep stage before and after photostimulation of the
1243 LPAG^{Vglut2}-GiV pathway in Chr2-mCherry mice. Data are presented as mean \pm SEM.
1244 Each dot indicates data from a single mouse ($n = 4$). * $p < 0.05$, ** $p < 0.01$, compared
1245 to the base group (**n-u**), using repeated measures ANOVA followed by a paired t-test
1246 (**r-t**) or paired t-test (**n-q, u**).
1247



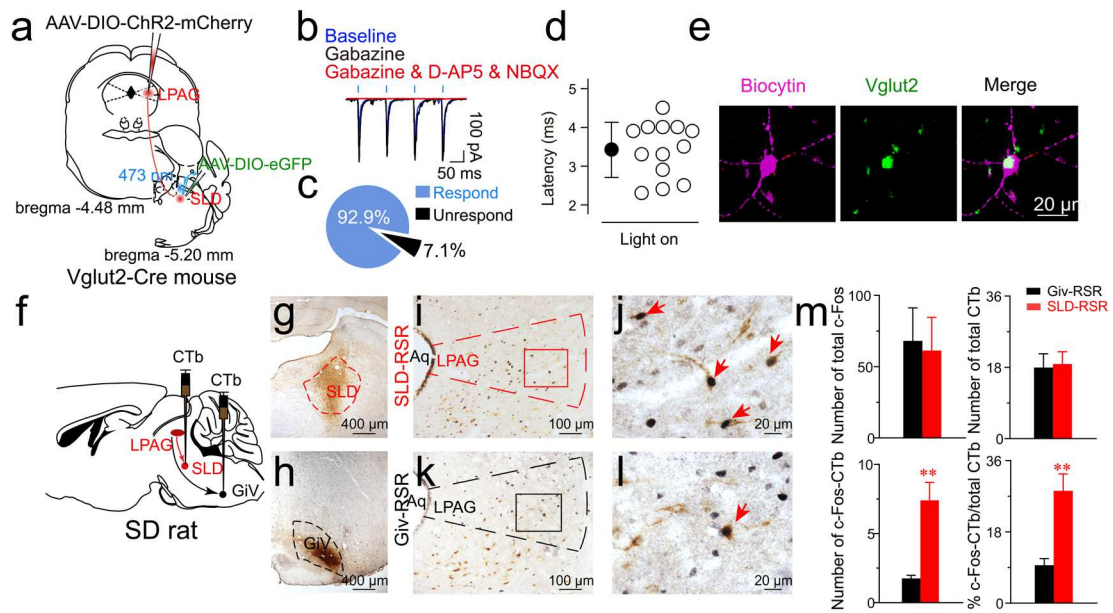
1248

1249 **Fig. 7 Chemogenetic inhibition of LPAG^{Vglut2} neurons decreases REM sleep and**
 1250 **increases NREM sleep.** **a** Vglut2-Cre mice were infused with AAV expressing hM4Di
 1251 in a Cre-dependent manner under the control of the Vglut2 promoter. **b** Diagrams of
 1252 superimposed AAV-injected areas in the LPAG of Vglut2-Cre mice ($n = 8$, indicated

1253 with different colors). **c** Typical traces of an hM4Di-expressing LPAG Vglut2 neuron
1254 bath applied with CNO) at a concentration of 5 μ M. **d, e** Firing frequency (**d**) and
1255 membrane potential (**e**) from CNO (5 μ M) application to the electrophysiological bath
1256 in five Vglut2 neurons. **f, g, h, i** Typical samples of two LPAG-hM4Di mice injected
1257 with either vehicle (**f, g**) or CNO (**h, i**). The full line rectangle area in **f** and **h** were
1258 magnified (**g, i**) to show the co-expression of hM4Di fusion protein mCherry and c-Fos,
1259 which is indicated by red arrows. **j, k** Typical examples of one LPAG-hM4Di mouse
1260 injected (i.p.) with vehicle (**j**) and CNO at 1 mg/kg (**k**). **l** Time course of REM sleep,
1261 NREM sleep, and wakefulness in Vglut2-Cre mice expressing hM4Di after
1262 administration of vehicle or CNO. **m** The total time spent in REM sleep, NREM sleep,
1263 and wakefulness in Vglut2-Cre mice expressing hM4Di for 3 h after administration of
1264 vehicle or CNO. **n** EEG power density for 3 h after administration of vehicle or CNO.
1265 The power of each 0.25-Hz bin was averaged and normalized by calculating the
1266 percentage of each bin from the total power (0–24.75 Hz). **o** The locomotor activity in
1267 Vglut2-Cre mice expressing hM4Di for 15 min after administration of vehicle or CNO.
1268 **p** A representative trajectory plot of a Vglut2-Cre mouse after administration of vehicle
1269 or CNO. **q** Mean immobility time in Vglut2-Cre mice expressing hM4Di for 15 min
1270 after administration of vehicle or CNO. Data are presented as mean \pm SEM ($n = 6-10$).
1271 Each dot indicates data from a single mouse. * $p < 0.05$, ** $p < 0.01$ compared to the
1272 vehicle group, using repeated measures ANOVA followed by a paired t -test (**l**) or a
1273 paired t -test (**m**).

1274

1275



1276

1277 **Fig. 8 LPAG^{Vglut2} neurons were activated during REM sleep through the**
 1278 **projections to the SLD.** **a** Schematic of the experiment. AAV-ChR2 was injected into
 1279 the LPAG of Vglut2-Cre mice, and the response was recorded in the SLD. **b** Typical
 1280 traces representing the inward current elicited by photostimulation of ChR2-expressing
 1281 LPAG axons at the SLD under different conditions. **c** The proportion of recorded SLD
 1282 neurons that did and did not respond to the photostimulation of ChR2-expressing LPAG
 1283 terminals. **d** The latency between delivery of photostimulation and the firing event of
 1284 the responding SLD neurons are summarized. **e** Typical example of a connected
 1285 biocytin-labeled neuron that was Vglut2-positive. Scale bar: 20 μ m. **f** Scheme of the
 1286 injection of CTb in rats that were submitted to 72-h protocol of REM sleep rebound
 1287 (RSR). **g, h** Photomicrographs illustrating representative injection sites in the SLD (**g**)
 1288 and the GiV (**h**). **i-l** Low- (**i, k**) and high-power (**j, l**) photomicrographs showing the
 1289 LPAG neurons active after RSR and projecting to the SLD (**i, j**) and GiV (**k, l**). **j** and **l**
 1290 show the area inside the rectangle in **i** and **k** at a higher magnification. Arrows indicate
 1291 double-stained neurons (c-Fos+/CTb+). **m** Histogram showing the numbers of total c-
 1292 Fos+ and CTb+ neurons and the percentage of double-labeled neurons within LPAG
 1293 for each experimental condition (SLD-RSR rats, $n = 4$; GiV-RSR rats, $n = 4$). ** $p <$

1294 0.01 compared to GiV-RSR animals, using one-way ANOVA followed by Tukey's post
1295 hoc test.

Supplementary Files

This is a list of supplementary files associated with this preprint. Click to download.

- [Fig.S1.pdf](#)
- [Fig.S2.pdf](#)
- [Fig.S3.pdf](#)
- [Fig.S4.pdf](#)
- [Supplementarymaterials.pdf](#)